Turbulent diffusivity profiles on the shelf and slope at the southern edge of the Canada Basin

Ruby Yee[1], Ruth Musgrave[1,2], Elizabeth Fine[3], Jonathan Nash[4], Louis St. Laurent[5], Robert Pickart[2]

[1]Dalhousie University Department of Oceanography, Halifax, NS, Canada
[2]Woods Hole Oceanographic Institute, Falmouth, MA, United States
[3]Scripps Institution of Oceanography, La Jolla, CA, United States
[4]Oregon State University College of Earth, Ocean, and Atmospheric Sciences, Corvallis, OR, United States
[5]University of Washington Applied Physics Laboratory, Seattle, WA, United States

Key Points:

- Average turbulent temperature diffusivity is elevated by 1-2 orders of magnitude on the shelf compared to over the deep slope
- A similar magnitude ($\mathcal{O}(1\ \mathrm{Wm}^{-2})$) of heat is fluxed into the cold halocline from the Atlantic Water below as from the overlying surface layer
- Heat fluxes as high as 50 Wm^{-2} are occasionally observed in the surface layer

Corresponding author: Ruby Yee, r.yee@dal.ca

Abstract

Vertical profiles of temperature microstructure at 95 stations were obtained over the Beaufort shelf and shelfbreak in the southern Canada Basin during a November 2018 research cruise. Two methods for estimating the dissipation rates of temperature variance and turbulent kinetic energy were compared using this dataset. Both methods require fitting a theoretical spectrum to observed temperature gradient spectra, but differ in their assumptions. The two methods agree for calculations of the dissipation rate of temperature variance, but not for that of turbulent kinetic energy. After applying a rigorous data rejection framework, estimates of turbulent diffusivity and heat flux are made across different depth ranges. The turbulent diffusivity of temperature is typically enhanced by about one order of magnitude in profiles on the shelf compared to near the shelfbreak, and similarly near the shelfbreak compared to profiles with bottom depth >1000 m. Depth bin means are shown to vary depending on the averaging method (geometric means tend to be smaller than arithmetic means and maximum likelihood estimates). The statistical distributions of heat flux within the surface, cold halocline, and Atlantic water layer change with depth. Heat fluxes are typically <1 Wm^{-2}, but are greater than 50 Wm^{-2} in ∼8% of the overall data. These largest fluxes are located almost exclusively within the surface layer, where temperature gradients can be large.

Plain Language Summary

In the Arctic Ocean, the mixing of water masses due to turbulence has important impacts on heat transport, influencing sea ice formation and loss. In this study, we quantify mixing using vertical profiles of temperature measured at high spatial resolution that were obtained during a November 2018 research cruise near the shelf and shelfbreak of the Canada Basin. We compare two methods for performing this estimation, and evaluate scenarios when either method might fail. Turbulent mixing rates are found to be higher over the shelf compared to the shelfbreak, and higher over the shelfbreak than the deep ocean, possibly due to interactions between currents and bottom topography. We also quantify rates of heat transport through three distinct water masses (the surface layer, a cold subsurface layer, and a warm water mass originating from the Atlantic Ocean). These findings are valuable for constraining Arctic Ocean heat budgets, as well as for establishing best practices when estimating turbulent mixing from high resolution temperature profiles.

1 Introduction

Turbulent diffusion plays a critical role in ocean mixing. Turbulent fluxes of dynamic tracers such as heat and salt set interior stratification, while fluxes of passive tracers such as nutrients and oxygen play an important role in the ocean's biogeochemistry (e.g., Yu et al., 2019; Warner & Moum, 2019; Freilich & Mahadevan, 2019; Uchida et al., 2019; Brandt et al., 2015; Gnanadesikan et al., 2012). On a larger scale, oceanic circulation and thus global climate is sensitive to turbulent diffusivities (Melet et al., 2022). Although the impacts can be seen at these largest spatial scales, the turbulent processes themselves occur at much smaller scales that can be difficult to resolve in conventional field measurements.

1.1 Diffusivities in the Arctic Ocean

Compared to other ocean basins, the Arctic Ocean has relatively low levels of turbulence, due in part to its strong near-surface stratification, which inhibits turbulence and vertical mixing. The presence of sea ice can also inhibit turbulence by limiting wind-driven energy input (Morison et al., 1985; Rainville & Woodgate, 2009). Rainville and Winsor (2008), for instance, observed turbulent diffusivities in the range of 10^{-6}–10^{-4}

m^2s^{-1} over the Lomonosov Ridge, in contrast to average diffusivities of 10^{-5}–10^{-3} m^2s^{-1} (and even higher near the bottom) across ridges in the non-polar global ocean noted by Waterhouse et al. (2014). In the cold halocline of the Amundsen Basin, Fer (2009) reported typical turbulent temperature diffusivities of $10^{-6} - 10^{-5}$ m^2s^{-1}. Double diffusion is a dominant mechanism for vertical mixing in many of the central Arctic basins; in the Laptev Sea, for instance, double diffusive staircases may be prevalent and associated with low turbulence away from the continental slope, while elevated turbulent diffusivities $> 10^{-4}$ m^2s^{-1} have been observed in bottom boundary layers on the shelf (Lenn et al., 2009, 2011).

This work focuses specifically on the Canada Basin, where heat fluxes can influence sea ice growth and retreat, in turn affecting mechanisms that generate turbulence. A reduction in sea ice during the last decade in this region has, for instance, contributed to increasing the energy of the near-inertial internal wave field (Dosser & Rainville, 2016). Pan-Arctic changes in turbulent dissipation and heat flux, likely associated with increased energy transfer from wind, have already been observed over the past decade (Dosser et al., 2021), although any link between sea ice loss and increased turbulence in the western Arctic Ocean has yet to be established (Fine & Cole, 2022). Nonetheless, vertical fluxes are especially relevant as enhanced upward heat flux can delay freezing, leading to shorter periods of the year when ice is present and less ice overall by the end of the winter.

Close to the coast, a number of water masses and currents coexist. Fig. 1 shows the potential temperature and absolute geostrophic currents (calculated as described in the next section) along one example cross-shelf transect (see Fig. 2 for the location). Prior observations indicate enhanced turbulent mixing over the shelfbreak, most likely due to the tides (Lincoln et al., 2016). Warm Pacific summer water (PSW) flows through Bering Strait and across the Chukchi Sea via different flow branches that ultimately enter the Canada Basin via Barrow Canyon (Lin et al., 2019). Upon exiting the canyon, the flow splits into the westward-flowing Chukchi Slope Current and the eastward-flowing Beaufort Shelfbreak Jet as illustrated in Fig. 1 of Lin et al. (2021). Through much of the Canada Basin, the PSW remains near the surface, typically at depths < 100 m (Pickart et al., 2009). In the past several decades, increasing heat content of the PSW delivered via Bering Strait has been correlated with a receding sea ice edge in the Canada Basin (Timmermans et al., 2018; Woodgate et al., 2010). Heat transport dynamics in this region are further influenced by the warm and salty Atlantic water (AW) layer between 150-500 m depth, which is typically insulated from the surface by the cold halocline layer comprised of remnant Pacific winter water (Nikolopoulos et al., 2009; Timmermans & Marshall, 2019) (Fig. 1a).

1.2 Measuring turbulent diffusivity

Turbulence in the ocean acts at scales from cm to m by increasing gradients and enhancing the effect of molecular diffusion compared to a laminar flow. Direct methods for estimating turbulent diffusivity typically require measurements of microstructure shear, but shear measurements are easily contaminated by vibrations, and thus require specialized sampling platforms like free-falling profilers or gliders (Goto et al., 2016). As such, diffusivities are not typically or easily measured during research cruises, in contrast to the data obtained from more ubiquitous platforms like conductivity-temperature-depth (CTD) rosettes. As a result, diffusivity observations are sparse despite their importance for constraining models of global ocean circulation (Waterhouse et al., 2014; Simmons et al., 2004). While turbulence measurements are sparse globally, there are particularly few documented measurements in the Arctic Ocean (Waterhouse et al., 2014).

As an alternative to using microstructure shear, diffusivity can also be estimated from measurements of temperature microstructure (e.g., Luketina & Imberger, 2001; Rud-

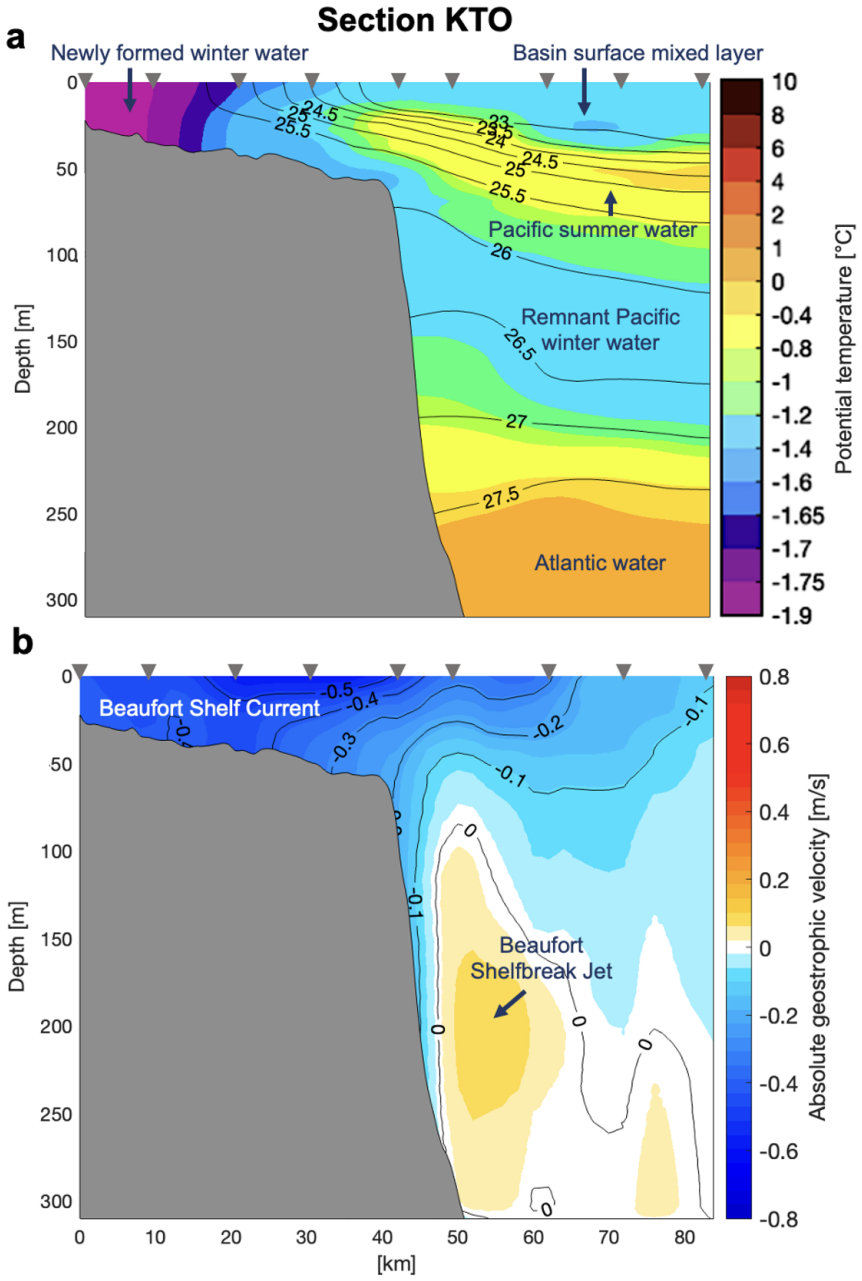

Figure 1. Vertical section of (a) background potential temperature (from the CTD) with contours of potential density (kg m^{-3}) overlain and (b) absolute geostrophic velocity (derived from the hull-mounted acoustic Doppler current profiler (ADCP)) for the example transect KTO (see Fig. 2 for the location of the transect). The major water masses and currents are identified. The station locations are indicated by the grey triangles. Bathymetry comes from the ship's echosounder, and a 2D spline interpolation was used to create these transects from the CTD and ADCP measurements.

dick et al., 2000; Moum & Nash, 2009; Scheifele et al., 2021; Goto et al., 2021). This approach has the advantage that measurements are not affected by platform vibrations to the same extent as shear-based methods. Fast-sampling temperature probes can thus be mounted onto a CTD rosette, making data collection readily accessible on most cruises where CTD profiles are already being made. Provided that appropriate corrections and quality controls are applied, turbulence estimates from both free-falling and CTD rosette-attached microstructure temperature profilers have been shown to generally agree with concurrent shear-based estimates (Goto et al., 2016, 2018).

A key difficulty when using temperature microstructure is that the Batchelor length scale, where the molecular diffusion of temperature becomes the dominant process, is smaller than the Kolmogorov length scale, where the viscous dissipation of turbulent kinetic energy becomes dominant. Estimates of turbulent parameters ideally require that the full turbulence subrange down to the Kolmogorov and Batchelor scales is resolved. This means that for a given sampling rate, profiling instruments that measure temperature microstructure must maintain slower descent rates in order to resolve the Batchelor length scale than would be necessary when measuring shear microstructure.

The two key goals of this work are 1) to explore options for turbulence data collection using temperature microstructure collected from a CTD rosette, and 2) to describe the spatial distribution of turbulent diffusivities and heat fluxes over the shelf and slope of the southern Canada Basin. Specifically, we present a novel comparison of two methods for calculating turbulent diffusivities and establish data rejection criteria for each method that account for differences between observed and theoretical turbulent spectra, the sudden deceleration of the rosette, low signal to noise ratios and differences between the methods. Our quality controlled dataset is then used to estimate the spatial structure of turbulent diffusivities and heat fluxes across the shelf and slope, showing enhanced diffusivities in shallower waters, and quantifying the rate of heating of the cold halocline waters by both surface and Atlantic Waters at the time of the observations.

The dataset is described in Section 2. Section 3 presents the two methods for estimating turbulent diffusivities from temperature microstructure and details the rejection criteria appropriate for measurements obtained from a CTD rosette. The statistics and spatial distributions of temperature diffusivity and heat flux in the region are described in Section 4. Conclusions follow in Section 5.

2 Data

A research cruise aboard the USCGC *Healy* took place in the Canada Basin in October-November 2018, with the primary goal of studying the boundary current system. A Rockland Scientific MicroRider-1000 (referred to as MR from this point onward) was attached to a rosette alongside a Sea-Bird 911+ CTD. The MR is a self-contained turbulence profiler with two FP07 thermistor probes, which each sample temperature at 512 Hz. The sampling capabilities and physical setup of the MR attached to a CTD rosette are very similar to the χpods of Moum and Nash (2009). χpods are small, self-contained instruments equipped with fast response thermistors and accelerometers to measure instrument motion; they have previously been used for turbulence studies on moorings (e.g., Moum et al., 2013) and on lowered CTDs (e.g., Holmes et al., 2016; Lele et al., 2021). Although the MR is capable of recording microstructure shear, this functionality was not exploited during this cruise since the signal would have been contaminated by vibrations of the rosette.

CTD profiles and measurements of temperature microstructure were made on the shelf, slope, and farther offshore. These profiles comprise of 12 cross-shelf sections in addition to one section across Barrow Canyon on the northeast Chukchi shelf (Fig. 2). In total, 95 MR profiles and 133 CTD profiles with temperature and salinity binned to 1

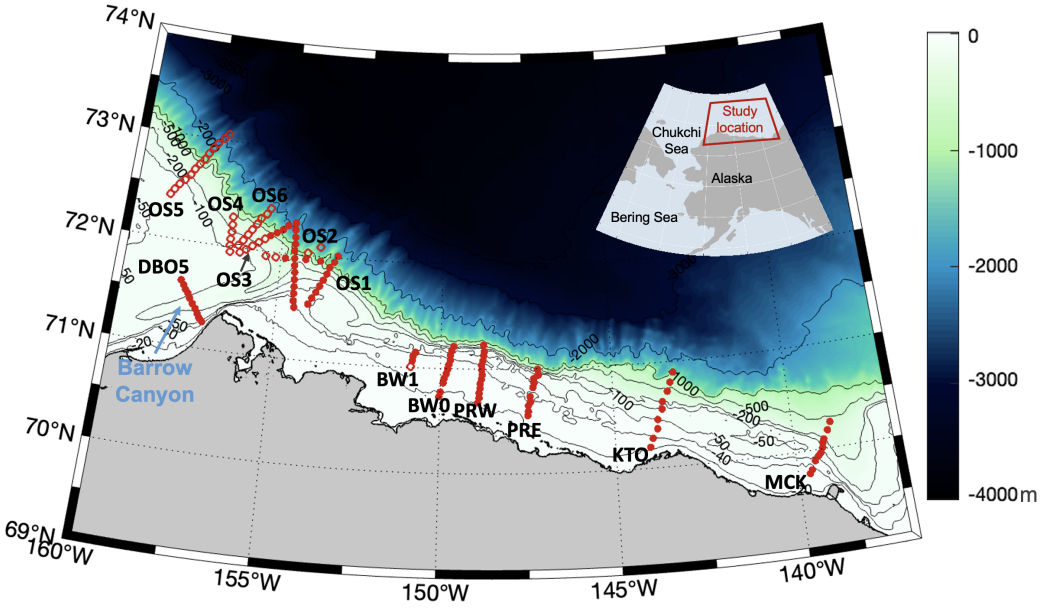

Figure 2. Map of the study area with transect names and inset indicating study location. Solid circles indicate profiles where temperature microstructure and CTD data are available. Open circles indicate profiles where only CTD data are available due to thermistor malfunction. Bottom depths come from IBCAOv3 (Jakobsson et al., 2012). Contour lines indicate bottom depth in metres.

m resolution were obtained (38 MR profiles were rejected due to sensor malfunction; at these locations, only CTD data are available). Microscale temperature was recorded by two thermistors on the MR (Ch1 and Ch2). All results in this paper have been derived from Ch1 because slightly more data was retained from Ch1 after applying rejection criteria (Section 3), suggesting better data quality compared to the other channel.

Any portions of the profiles from depths < 10 m were excluded to avoid contamination by the ship's wake. Most profiles end in a period of stepped speed reduction. These portions were identified manually for each profile and were also excluded from the analysis. Because data were collected mostly on the shelf and in the vicinity of the shelfbreak, the maximum depth reached by these profiles ranges from 20-385 m, which is quite shallow compared to other open-ocean field studies. As a result, the descent speed of the rosette was generally slow, around 0.55 ms^{-1}, giving a nominal vertical resolution at 512 Hz of 0.1 cm.

Background vertical temperature gradient, $d\overline{T}/dz$, and squared buoyancy frequency,

$$N^2 = -\frac{g}{\rho_0}\frac{\partial \rho}{\partial z} \tag{1}$$

where ρ_0 is a reference density, g is gravitational acceleration, and $\partial\rho/\partial z$ is the vertical density gradient, were calculated using 1 m-binned temperature and salinity profiles obtained by the CTD. For both temperature and salinity, observations from two redundant sensors were averaged. Density overturns were seldom observed in 7 of the 133 CTD profiles. In data segments where overturns were present, N^2 was set to zero.

Direct velocity measurements were made during the cruise using an RDI Ocean Surveyor 150 kHz acoustic Doppler current profiler (ADCP) mounted on *Healy's* hull. The near-surface blanking region extended to roughly 18 m, and the bottom blanking typically extended 10 m above the seafloor. For details on the data acquisition and processing, the reader is referred to Dabrowski et al. (2022). The barotropic tidal signal was removed from the velocity profiles using the Oregon State University model (Padman & Erofeeva, 2004). Absolute geostrophic velocities were subsequently computed by referencing the CTD-derived thermal wind shear using the de-tided ADCP profiles, following the procedure described in Pickart et al. (2016).

3 Methods

3.1 Turbulence analysis

In the presence of turbulence, the frequency or wavenumber spectrum for such quantities as kinetic energy and temperature fluctuation gradient ($\nabla T'$) has been observed to follow a universal form that can be predicted by considering fluid convection and molecular diffusion (Batchelor, 1959). By fitting theoretical forms to observed $\nabla T'$ spectra, the turbulent parameters χ and ε—the rates of dissipation of temperature variance and turbulent kinetic energy, respectively—can be calculated, and, subsequently, turbulent diffusivities can be estimated. Theoretical forms for the $\nabla T'$ spectrum have been described by Batchelor (1959) and Kraichnan (1968). Both forms are similar in shape and scale similarly with χ and ε. The difference in χ recovered by integrating the Batchelor spectrum versus the Kraichnan spectrum is small. We use the Kraichnan spectrum in this paper for all computations.

We generate $\frac{\partial T'}{\partial z}$ wavenumber spectra using Rockland Scientific's ODAS MATLAB processing library following the methods described in Rockland Scientific's Technical Note 039 (Lueck et al., 2020). Only $\frac{\partial T}{\partial t}$ was measured, but $\frac{\partial T}{\partial z}$ was obtained by assuming a constant descent rate over each spectral window (within each 2 s window, descent rate varies by only 1-2%). Wavenumbers are obtained by dividing frequencies by the constant descent rate. Because the background gradient varies much more slowly than the fluctuations, we take $\frac{\partial T}{\partial z} = \frac{\partial T'}{\partial z}$. The turbulence is assumed to be isotropic such that the magnitudes of vertical variance also represent horizontal variance in temperature. Thus, we can make the approximation $(\nabla T')^2 = 3(\frac{\partial T'}{\partial z})^2$. Each spectrum is generated from 2 s of data, and adjacent spectral windows overlap by 1 s.

Several stages of electronic signal processing within the MR contribute noise to the signal, according to known functions for noise outputs from each electronic component. The noise spectrum varies with profiling speed and temperature gradient, so noise is computed individually for each spectral window as described in Rockland Scientific's Technical Note 040 (Lueck, 2019).

We explore two methods for fitting theoretical $\nabla T'$ spectra to observations: the full spectrum (FS) method and the resolved wavenumber (RW) method. The following subsections describe each in detail. χ, the dissipation rate of temperature variance, is defined in the temperature variance equation as

$$\chi = 2\kappa(\overline{\nabla T')^2}, \tag{2}$$

where the overline indicates a time average, and κ is the molecular diffusivity of temperature, which varies with temperature, salinity, and pressure. Exploiting Parseval's theorem, χ can be calculated by integrating the fitted Kraichnan spectrum:

$$\chi = 6\kappa \int_0^\infty \Psi_{T_z'}(k)dk, \tag{3}$$

where k is wavenumber and $\Psi_{T'_z}(k)$ is the Kraichnan spectrum of the vertical temperature fluctuation gradient.

By assuming turbulence is steady, isotropic, and homogeneous, turbulent diffusivities can be estimated from either χ or turbulent kinetic energy dissipation rate, ε, as described in the following subsections. The resolved wavenumber method relies on the additional assumption that salt and density diffusivities are equal; thus, one diffusivity estimate referred to as κ_e ($\kappa_e = \kappa_T = \kappa_\rho$) is output, whereas the full spectrum method outputs two different-valued diffusivities (κ_T and κ_ρ). It is generally assumed that in regions where mixing is dominated by turbulence, the eddy diffusivity representing both salt and temperature is equal. However, Fer (2009) found that independent estimates of κ_T and κ_ρ were not always equal in the central Arctic Ocean away from boundaries, where turbulence is low.

Both of the methods assume the following: 1) T' arises only from turbulence; 2) only the environmental signal contributes to observed T'; 3) the turbulence is in steady state, such that the production rate is balanced by the dissipation rate of temperature variance; 4) the turbulence is homogeneous; and 5) the turbulence is isotropic. However, these assumptions are not always met. For instance, in locations that are already well-mixed in the vertical (e.g. highly turbulent boundary layers with low stratification and negligible background gradients), turbulence will be under-predicted since overturning motions will not produce gradients and will thus be invisible to the temperature sensors. Some non-environmental sources of T', such as from water entrained in the rosette, can violate assumption 2 and are considered in our spectral rejection criteria (Section 3.4). Assumptions 3-5 are necessary if Equations 3 (and all subsequent equations involving χ), 8, and 9 are to be used.

3.2 Full spectrum method

The most commonly used method for fitting theoretical turbulence spectra to oceanic temperature gradient spectra uses the entire observed spectrum to perform a Maximum Likelihood Estimate (MLE) fit. This method for obtaining turbulent parameters from temperature microstructure was first detailed by Ruddick et al. (2000) and has since been applied in other studies (e.g., Goto et al., 2021; Scheifele et al., 2018). Unlike a traditional least squares fit, the maximum likelihood approach is unbiased even when the errors are non-Gaussian (Ruddick et al., 2000). We will henceforth refer to the method described in this section, which utilizes Ruddick et al. (2000)'s MLE approach, as the full-spectrum (FS) method.

The dissipation length scale for temperature variance, k_B^{-1} (where k_B is the Batchelor wavenumber), is not resolved in some cases: given typical ranges for ε, the dissipation rate of turbulent kinetic energy, in the western Arctic Ocean ($\sim 10^{-11}$ to $10^{-8}\mathrm{m}^2\mathrm{s}^{-3}$ as observed by, e.g., Scheifele et al. (2018)), Batchelor length scales around 1 to 0.1cm could be expected. The smallest length scales are thus at the limit of the typical $\mathcal{O}(0.1\mathrm{cm})$ resolutions obtained in this study based on descent rate and sampling frequency (Section 2). However, in practice these scales cannot be resolved due to limitations in the dynamic response of the FP07 thermistors at high frequencies, when ε exceeds $\sim 10^{-8}$ $\mathrm{m}^2\mathrm{s}^{-3}$, or during periods when the instrument descent rate was faster than the mean rate. Additional considerations on how descent rate may constrain estimates of ε can be found in Appendix B.

Because the FS method fits a theoretical spectrum to the entire range of observed wavenumbers (even those that are noise-contaminated or only partially resolved), some adjustments to the original data must be made to try to compensate for the measured signal rolling off prematurely at high wavenumbers (e.g., Goto et al., 2016; Bluteau et al., 2017). As such, observations are boosted by dividing the observed spectrum by the double-pole FP07 transfer function from Gregg and Meagher (1980):

$$H(f) = [1 + (2\pi\tau f)^2]^{-2}, \tag{4}$$

where τ is the time constant required for a $1-e^{-1}$ rise in signal and f is frequency in Hz. However, because FP07s are handmade, they differ from one another in glass thickness and shape, and, as a result, in time response (Gregg & Meagher, 1980). As it is not practical to measure τ for individual sensors, we follow Goto et al. (2021) by using a fixed time constant of $\tau = 3$ ms, which is consistent (within about a factor of two) with typical values used in the literature (e.g., Gregg & Meagher, 1980; Nash et al., 1999).

When the observed spectrum is boosted with the transfer function, the noise—which contributes to the overall observed signal—is also boosted. For this reason, the transfer function is also applied to the estimated noise spectrum (see Section 3.1) and the boosted noise is added to the theoretical turbulence spectrum, prior to fitting to observations:

$$\Psi_{fit} = \Psi_{Kraichnan} + \frac{\Psi_{noise}}{H(f)}, \tag{5}$$

where the theoretical spectrum that is fit to observations, the Kraichnan spectrum, and the noise spectrum are represented by Ψ_{fit}, $\Psi_{Kraichnan}$, and Ψ_{noise}, respectively. The boosted noise spectrum is then subtracted before integrating for χ.

The FS method, detailed in Ruddick et al. (2000), uses a fitting algorithm wherein the Batchelor wavenumber, k_B, is adjusted while the value of χ is set by the integral of the observed spectrum minus the noise spectrum. The k_B corresponding to the Kraichnan spectrum that is the most likely theoretical form for the observation is selected.

The Batchelor wavenumber corresponds to the length scale at which molecular diffusion of temperature becomes effective. ε is related to k_B as

$$\varepsilon = (2\pi k_B)^4 \nu \kappa^2, \tag{6}$$

where ν is the kinematic viscosity, which varies with temperature, salinity, and pressure (Batchelor, 1959). The turbulent diffusivities of temperature and density, κ_T and κ_ρ, are then calculated. κ_T depends on χ as

$$\kappa_T = \frac{\frac{1}{2}\chi}{\left(\frac{d\overline{T}}{dz}\right)^2}, \tag{7}$$

assuming a balance between production and dissipation in the temperature variance equation (Osborn & Cox, 1972). κ_ρ depends on ε as

$$\kappa_\rho = \frac{\Gamma\varepsilon}{N^2}, \tag{8}$$

assuming a balance between shear production, buoyancy production, and turbulent dissipation in the turbulent kinetic energy equation (Osborn, 1980). Γ is often referred to as the mixing efficiency, and a value of $\Gamma = 0.2$ is used (Moum, 1996; St. Laurent & Schmitt, 1999).

Descent rate limits the wavenumbers resolvable by the sensors—higher descent rates cause smaller spatial scales to be unresolved. Calculations of ε from the FS method (ε_{FS}) can be affected by descent rate resolvability because ε depends on k_B, which typically occurs towards or even past the lower spatial limit of resolution. The issue of resolvability limits on ε_{FS} due to descent rate is discussed in Appendix B.

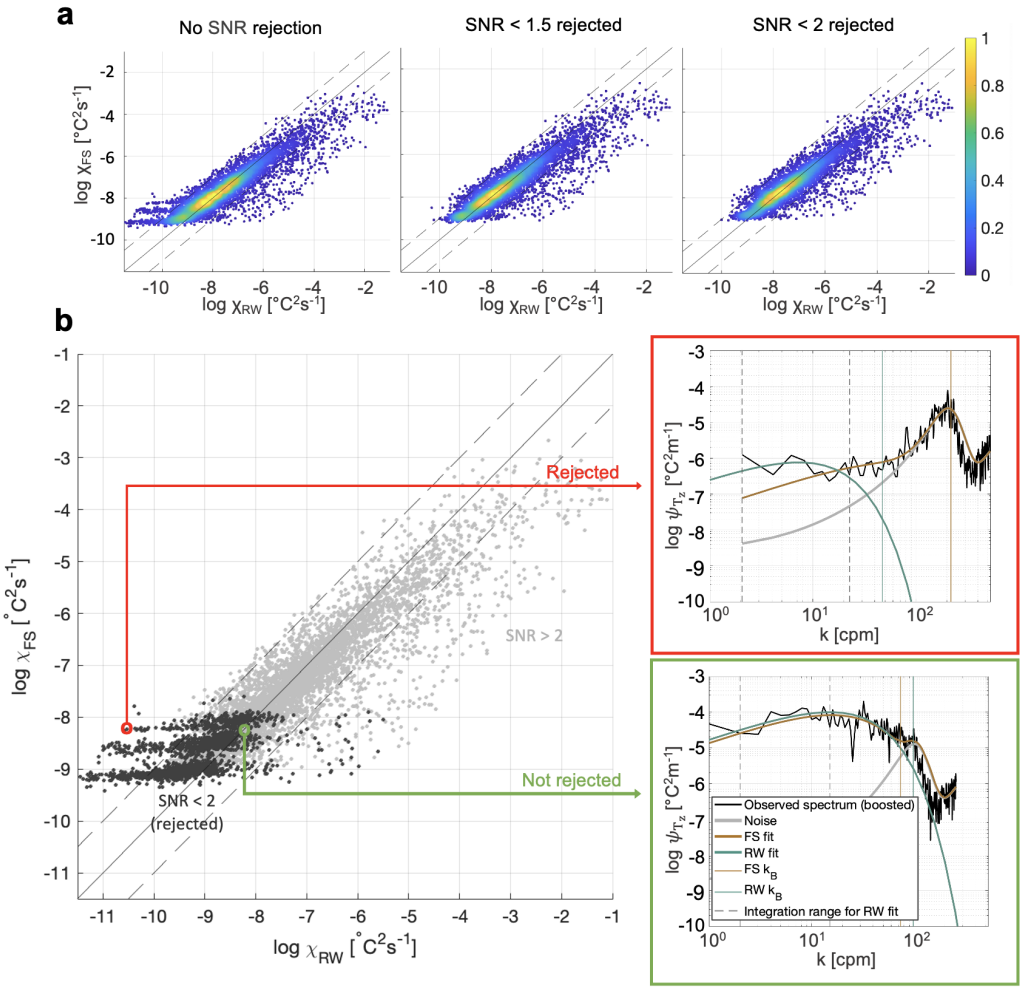

Figure 3. a) Comparison of χ calculated using the FS and RW methods for no signal-to-noise ratio (SNR) rejection, rejection for SNR<1.5, and rejection for SNR<2. Colour bar indicates relative point density. The solid one-to-one line indicates where the methods agree perfectly, and the dashed lines indicate one order of magnitude difference in χ between methods. b) For a rejection threshold of SNR<2, example rejected spectra (red box) and non-rejected spectra (green box) from both methods are shown to illustrate how differences in fit method affect estimation of χ.

An example FS fit to a boosted spectrum is shown inside the green box in Fig. 3 (thick brown line).

3.3 Resolved wavenumber method

To circumvent the difficulties in estimating the dynamic response of individual FP07 probes, Moum and Nash (2009) proposed an alternative to the FS method. Rather than fitting the theoretical spectrum to the entire range of observations, their method can be used to fit to the portion of the viscous-convective subrange in a range of wavenumbers where the spectrum is resolved. From here on, we will refer to this fitting method as the resolved wavenumber (RW) method.

The advantage of this technique is that noise and small scale resolvability need not be considered, since they affect only higher wavenumbers outside of the portion of the spectrum used to perform the fit. Thus the method makes no assumptions about the noise spectrum or transfer function. Moum and Nash (2009) previously used a sensor-dependent correction after measuring the time response of individual thermistors, but it is not necessary to do so when the upper frequency used for the fit is in the range of 10-15Hz (their fit range extended as high as 40Hz).

However, since the fit does not include the shape of the spectrum in the vicinity of the spectral roll-off, an additional assumption that $\kappa_T = \kappa_\rho$ is required for an unambiguous fit. This gives an expression for ε,

$$\varepsilon = \frac{N^2 \chi}{2\Gamma \left(\frac{d\overline{T}}{dz}\right)^2}, \tag{9}$$

which follows from Equations 7 and 8. A Kraichnan spectrum fit is obtained by requiring that the integral over the resolved part of the observed spectrum matches the integral of the Kraichnan spectrum over the same wavenumber range. Using the fitted spectrum, χ is calculated from Equation 3, and ε from Equation 9.

An example RW fit is shown inside the green box in Fig. 3 (thick teal line). The wavenumber range used to perform the fit is indicated by the dashed grey lines; the upper wavenumber is either $k_B/2$ or the wavenumber associated with a frequency of 15 Hz (whichever is smaller), and the lower wavenumber is either the smallest resolved wavenumber or 2 cpm (whichever is larger). The observed spectrum is unaffected by both instrument noise and roll off within this range, so noise does not need to be considered when using the RW method.

3.4 Rejection criteria

In order to establish confidence in the results, criteria for removing contaminated or untrustworthy spectra are required. This is also necessary for a rigorous comparison of the FS and RW methods. Data rejection is achieved using several criteria described briefly in this subsection. For further details on the criteria, including how the rejection thresholds for each criterion were chosen, see Appendix A. If a spectrum triggers one or more of the rejection criteria, it is excluded from further analysis.

Rejection by spectral misfit: The mean absolute deviation (MAD) is a measure of spectral misfit that is used to reject spectra that do not resemble the theoretical Kraichnan form. MAD is defined

$$\mathrm{MAD} = \frac{1}{n} \sum_{k_i=k_1}^{k_n} \left| \frac{\Psi_{obs}}{\Psi_{th}} - \left\langle \frac{\Psi_{obs}}{\Psi_{th}} \right\rangle \right|, \tag{10}$$

where Ψ_{obs} is the observed spectrum and Ψ_{th} is the corresponding fitted Kraichnan spectrum. n is the total number of wavenumbers, k_i, included in both the fitted and observed spectra. For both FS and RW methods, a spectrum is rejected if MAD > 1.4.

Rejection by descent speed: The MR was attached to a CTD rosette that entrains large volumes of water as it descends. During periods of abrupt deceleration, turbulent water that was entrained within the frame can overtake the probes, leading to high observed turbulence. Under some conditions, the MR may even reverse direction and briefly travel upwards, causing it to sample through its own turbulent wake (for example, during high wave conditions).

We define a descent speed threshold, w_t, that is adjustable with descent rate and is determined independently for each spectral window. The threshold is

$$w_t = 0.75 w_3, \tag{11}$$

where w_3 refers to the mean descent speed from the past 3 s of data (or since the start of the profile, for the first 3 s). Any spectrum with $w < w_t$ is rejected. All spectra from 1.5 s after w increases back above w_t are also rejected.

Rejection by SNR: In cases of weak turbulence or laminar flow, instrument noise can be comparable to or larger than the measured signal. The signal-to-noise ratio (SNR) is the ratio of the integral of the observed spectrum to the integral of the predicted noise spectrum, with both spectra having first been boosted by the double-pole correction of Gregg and Meagher (1980) (Equation 4). Spectra with SNR < 2 are rejected for both FS and RW methods. In the following analyses involving κ_T (Section 4.3), locations with SNR below the threshold are set to have diffusivity equal to the molecular value so long as $|d\overline{T}/dz| > 0.001$ °Cm^{-1} (see Section 4).

Rejection due to FS and RW disagreement: Given the different assumptions of the FS and RW method, we can establish confidence in our estimates when they both yield similar results. Accordingly, spectra that have greater than one order of magnitude difference between χ_{RW} and χ_{FS} are rejected.

4 Results and discussion

4.1 Rejection statistics

The proportion of all data rejected by each criterion are shown in Fig. 4. The overall proportion of data rejected by the MAD criterion is around 5% with the FS method and 6% with the RW method, suggesting that the fitting algorithms of both methods are similarly robust.

The percentage of rejected indices in this study is high compared to other studies. For instance, Scheifele et al. (2018) rejected 33.9% of their $\nabla T'$ spectra using the FS method to estimate ε. Here we reject 67.8 (66.3)% overall using the RW (FS) method. There are several reasons for such high levels of data rejection: more rejection criteria—other authors often consider one or two, but not all, of the criteria described here; the requirement for agreement between methods; low levels of turbulence in the Arctic Ocean environment, which corresponds with high levels of SNR rejection; and an abundance of shallow profiles (45 of 95 profiles were < 50m), from which a large proportion of data were rejected due to instrument deceleration, especially compared to the deep ocean where profiles tend to be longer and constant descent rates can be maintained for longer periods.

Low SNR is a major cause for rejection in this dataset. SNR-rejected spectra represent places where the signal may have been low enough that negligible turbulence and

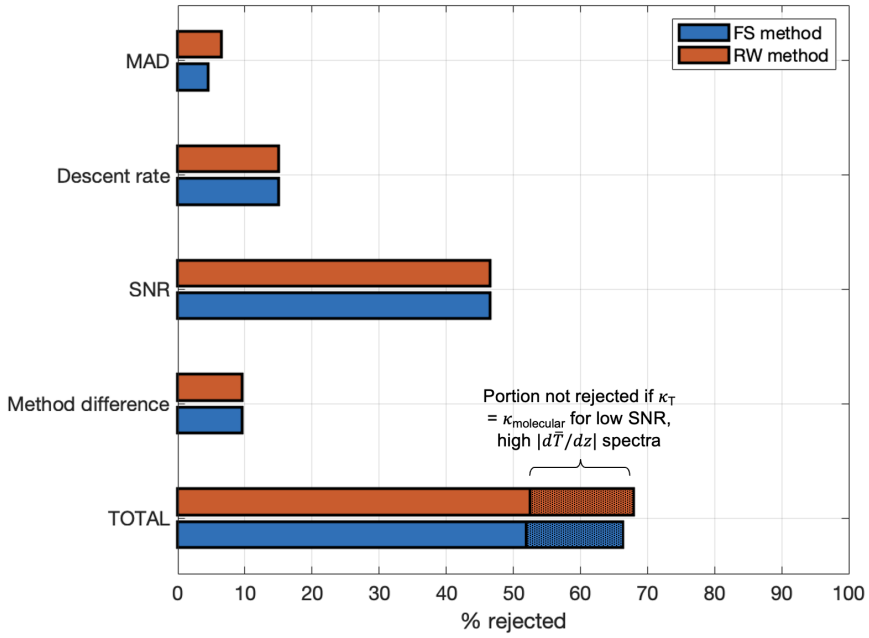

Figure 4. Percentage of spectra rejected due to the MAD, descent rate, and SNR rejection criteria. Other than MAD, the criteria are independent of method. The TOTAL rejected category refers to the percentage of spectra rejected by one or more of the other criteria. Imposing molecular values for turbulence parameters at all SNR-rejected locations with $|d\overline{T}/dz| > 0.001$ $^{\circ}\mathrm{Cm}^{-1}$ reduces the total rejected spectra by over 10% for each method (indicated by shaded areas on TOTAL bars).

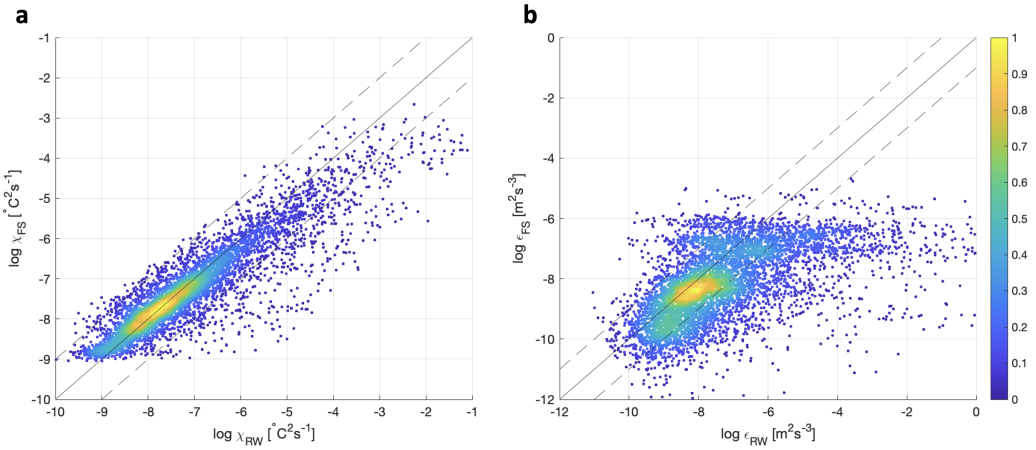

Figure 5. Comparison of a) χ_{FS} versus χ_{RW} and b) ε_{FS} versus ε_{RW}. The data have been quality controlled using all rejection criteria except rejection due to FS/RW disagreement. Colour indicates relative point density. The solid line indicates the one-to-one line, and dashed lines indicate one order of magnitude deviation from the one-to-one line.

effectively laminar flow can be assumed. It is not surprising that SNR is the dominant cause of rejection in this data set, since turbulence is highly intermittent in space and time (Cael & Mashayek, 2021). However, an inherent limitation when using scalar spectra to estimate turbulence is that low SNR can also occur due to an absence of background gradients, regardless of the strength of turbulence. Thus, we assume that diffusivities are dominated by molecular values, i.e. $\kappa_T = \kappa$, only when two conditions are met: 1) SNR is below the rejection threshold and 2) $|d\overline{T}/dz| > 0.001$ °Cm^{-1}, a threshold chosen based on the difference in distribution of $|d\overline{T}/dz|$ associated with SNR-rejected spectra compared to all $|d\overline{T}/dz|$ measurements. After imposing molecular diffusivity at these locations, the total data rejected is 52.4 (51.4)% overall for the RW (FS) method—a reduction by over 10% for both methods. Another benefit of assigning a molecular value to low SNR, high $|d\overline{T}/dz|$ spectra is to reduce the bias in properties averaged over multiple profiles, which otherwise would include only measurements in actively turbulent regions. However, this approach may result in slightly underestimated κ_T overall, since some spectra rejected by SNR could have very low diffusivity without necessarily being at the molecular level.

4.2 Establishing confidence in χ

After applying all rejection criteria (except for rejection due to FS and RW disagreement), we found that the two methods agreed within one order of magnitude 87.7% of the time for χ, but only 53.2% of the time for ε (Fig. 5). This is because of differences in the assumptions about the turbulent cascade that affect the estimation of ε: in the FS method ε is calculated from k_B, which is instantaneously proportional to the turbulent strain rate of the smallest eddies. In the RW method ε is related to spectral levels in a way that is applicable to a time- or space-averaged turbulent mixing event such that Γ can be reasonably assumed to take a constant value, and that $\kappa_\rho = \kappa_T$. In contrast, χ is calculated the same way in each method by integrating the fitted theoretical spectrum.

Background conditions can affect the validity of assumptions necessary for estimating ε, which differ in each method. The RW method assumes constant Γ, which may be violated, especially in locations where dissipation is driven by double diffusion (DD) (Inoue

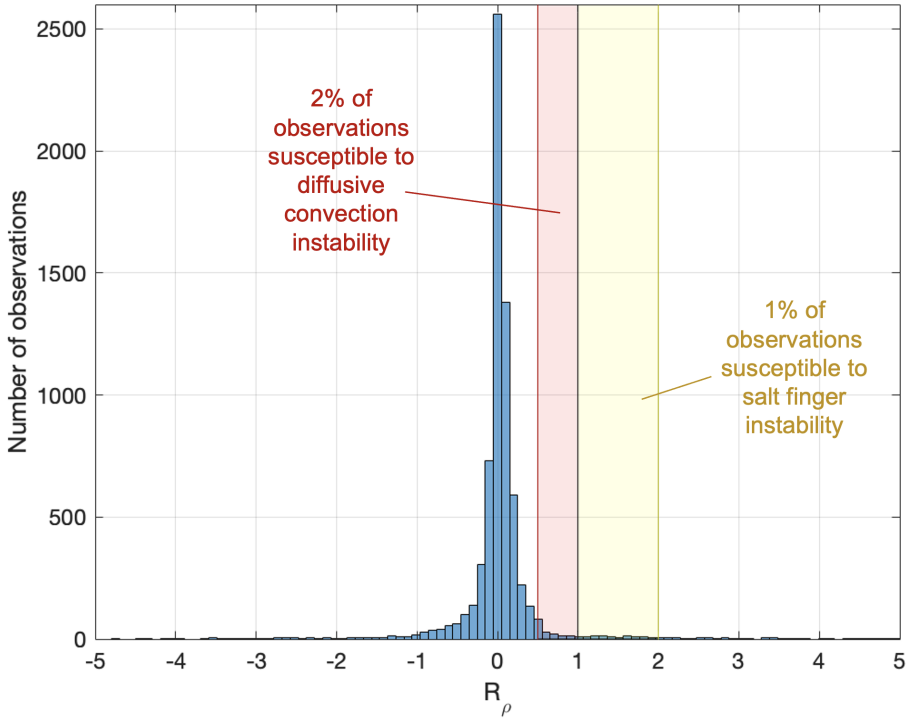

Figure 6. Distribution of the density ratio, R_ρ, for all non-rejected observations. Approximately 2% of data is in the diffusive convection susceptible regime ($0.5 < R_\rho < 1$), and approximately 1% is in the salt finger regime ($1 < R_\rho < 2$).

et al., 2007; Polyakov et al., 2019). The density ratio, $R_\rho = (\alpha\overline{\frac{\partial T}{\partial z}})/(\beta\overline{\frac{\partial S}{\partial z}})$, where α and β are the coefficients of thermal expansion and haline contraction, can be used to identify regions susceptible to instability by DD. We follow Merrifield et al. (2016) who, based on Schmitt (1979), estimate that DD instabilities with growth rates exceeding the buoyancy period can develop for $0.5 < R_\rho < 2$, where $0.5 < R_\rho < 1$ is the susceptible range for diffusive convection instability, and $1 < R_\rho < 2$ is susceptible to salt fingering. Of the non-rejected observations in this dataset, only about 2% are within the diffusive convective range, and 1% are in the salt finger range (Fig. 6). Nearly all of the salt finger-susceptible R_ρ in this dataset were observed in the upper 100 m, where warm summer Pacific water overlies cooler and relatively fresher remnant winter water. Although conditions are sometimes susceptible to the growth of DD instabilities, they may not develop if sufficiently strong turbulent mixing disrupts layer formation (St. Laurent & Schmitt, 1999). In this dataset, DD steps are not present and it is unlikely that DD was responsible for significant temperature variance, unlike in the central Canada Basin where DD is often observed (e.g., Timmermans et al., 2008; Padman & Dillon, 1989).

Challenges associated with measuring high wavenumber temperature variance at the descent rates used during the cruise can also limit our confidence in the FS fits for ε, especially for determining k_B, which is the wavenumber at which the spectrum rolls off and thus depends on both the turbulence and the unknown time-response of the thermistor. Because of the fourth-order k_B dependence in Equation 6, a factor of two uncertainty in τ produces a factor of 16 uncertainty in ε.

Given the large differences in ε and our inability to identify whether either method is more accurate, we focus only on χ going forward. The FS fit depends on both χ and

ε, so errors in ε may contribute to errors in χ. However, the effect on χ of varying ε is mitigated by applying the FS and RW disagreement rejection criterion described in Section 3.4, since a χ_{FS} significantly affected by errors in ε_{FS} will be rejected on the basis of disagreement with χ_{RW}.

4.3 Spatial patterns of turbulent temperature diffusivity

Three transects of κ_T give some insight into the patterns and variability of shelf and shelf-break turbulence in the region (Fig. 7). Although only $\kappa_{T,FS}$ is depicted, similar patterns and magnitudes are obtained using $\kappa_{T,RW}$.

Diffusivity tends to be large ($> 10^{-4}$ m^{2}s^{-1}) in the upper 50-75 m, above the cold halocline. These shallowest waters may be subject to mixing by wind and bottom-enhanced turbulence on the shelf. Few sections included non-rejected MR data beyond the depth of the shelf, however, two transects (OS2 and KTO) include data available down to 300 m. These two transects exhibit considerably patchy κ_T through the cold halocline and the AW, with values ranging from the molecular level up to $\mathcal{O}(10^{-4})$ m^{2}s^{-1} (Fig. 7 a,c). Interestingly, a region of elevated κ_T in Fig. 7c is located mostly within the $0 \mathrm{m} s^{-1}$ velocity contour, where geostrophic shears are weak. In general, no correlation between Richardson number (Ri) and κ_T was observed. However, our estimates of Ri are limited by the resolution of the ADCP velocities (4 m vertical resolution with 18 m surface blanking), which could mean that the velocity length scales used to calculate Ri were too large to capture instabilities that give rise to elevated κ_T.

Patches of low diffusivity (near 10^{-7} m^{2}s^{-1}) are not uncommon, especially within the AW layer (e.g. Fig. 7c). κ_T estimates are not included for the shallowest shelf waters in most transects, where SNR is below the rejection threshold and $d\overline{T}/dz$ is too low to characterize diffusivity with this method. In these locations, it is hypothesized that the energetic conditions of the shelf environment have caused the water to be well-mixed, and thus the method of using scalar spectra for turbulence estimation cannot be applied.

The statistical distribution of κ_T is shown in Fig. 8 with depth ranges that correspond to $d\overline{T}/dz$ regimes from Fig. 10. Fig. 8 shows values estimated using the FS method. Values of $\kappa_T > 10^{-1}$ m^{2}s^{-1} (1% of all κ_T) have been excluded, since they have unphysically large values. Although this cutoff is somewhat arbitrary, it is imposed to control for non-physical values that have evaded all rejection criteria. κ_T tends to follow a log-skew-normal distribution with a tail towards higher values. This is consistent with Cael and Mashayek (2021), who observed that the log-skew-normal distribution is often most appropriate for turbulent processes. However, the distribution of $\kappa_{T,FS}$ near the surface (0-80 m) does not exhibit a clear peak, but rather plateaus between 5×10^{-2} and 5×10^{-5} m^{2}s^{-1}. A distinct peak around 10^{-5} m^{2}s^{-1} is seen below 80 m. The distribution of $\kappa_{T,RW}$ (not shown) is similar.

The elevated values of κ_T at depths greater than 160 m arise from a single profile at the northernmost end of section PRE near 147°W (Fig 2). This profile exhibited $\kappa_T \sim 10^{-2}$ m^{2}s^{-1} from around 340 m to the end of the cast at 375 m, which was 75 m above the sea floor. This portion of the profile exhibited very low $d\overline{T}/dz$, potentially due to bottom boundary-enhanced turbulence in proximity to the Beaufort Shelfbreak Jet, which is known to be especially energetic (Pickart et al., 2009; Spall et al., 2018). Except for this anomalous profile, κ_T tends to shift towards lower values with increasing depth.

To understand the relationship between turbulence and bathymetry in this region, we compared averaged profiles of κ_T on the shelf (defined as having bottom depths $\leq$50 m), shelfbreak (bottom depths from 50 to 1000 m), and over the deep slope (bottom depth $\geq$1000 m). Comparisons are sensitive to the averaging method (Schulz et al., 2023), and so depth-binned mean profiles created using an arithmetic average, a geometric average, and a maximum likelihood estimator for the expectation value (henceforth referred to

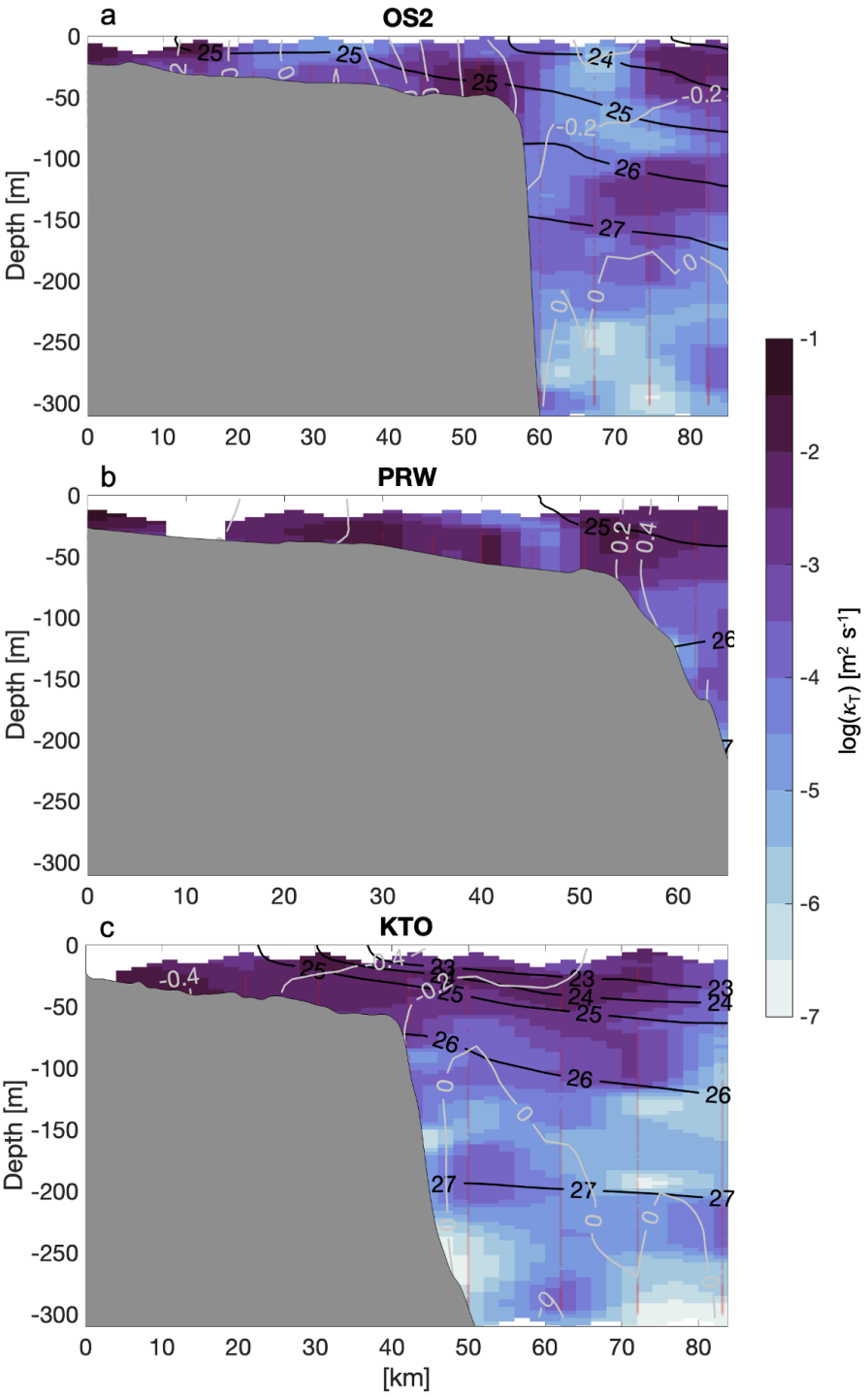

Figure 7. Transects of κ_T from the sections (a) OS2, (b) PRW, (c) KTO. Red dots indicate locations with non-rejected data used to interpolate the κ_T field. Contours of potential density (kg m^{-3}; black) and absolute geostrophic velocity (m s^{-1}; grey). Here κ_T is calculated using the FS method. Bathymetry comes from the ship's echosounder, and a 2D spline interpolation was used to create these transects from the MR profiles. Note differences in x-axis ranges.

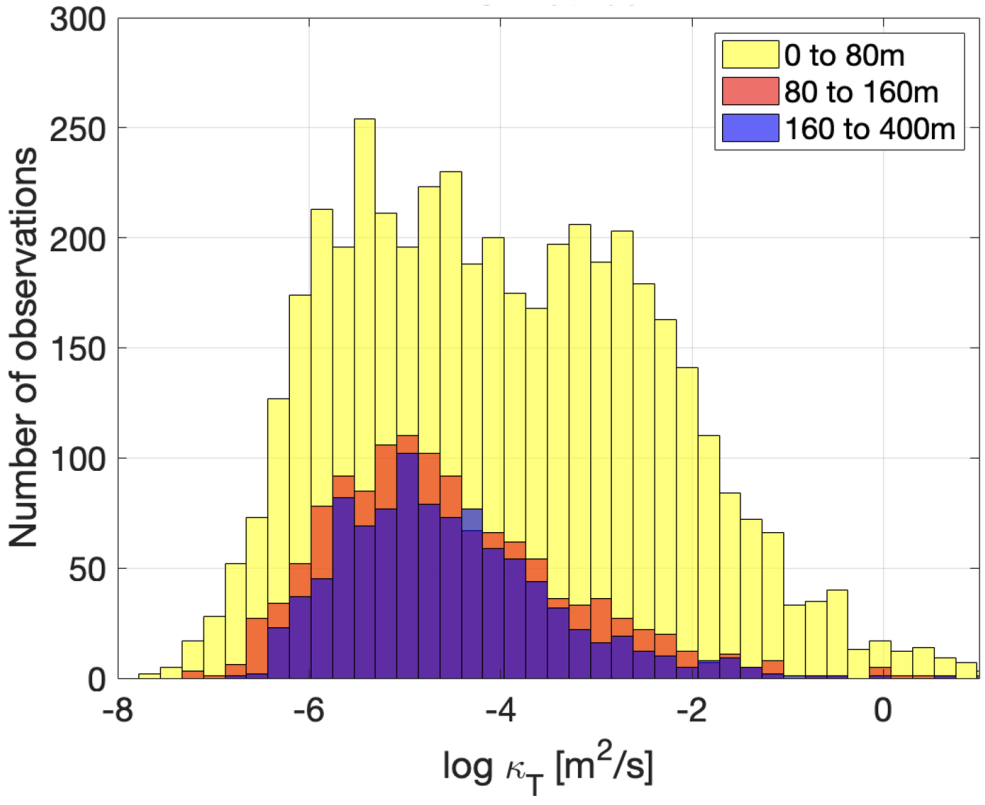

Figure 8. Distribution of κ_T, colour-coded by depth range (see legend). Note that values below 1.5×10^{-7} m^{2}s^{-1} are below the molecular diffusivity threshold and are thus non-physical, but have evaded all rejection criteria. Similarly, we consider $\kappa_T > 10^{-1}$ m^{2}s^{-1} to be non-physical and exclude them from further analysis. Here κ_T is calculated using the FS method.

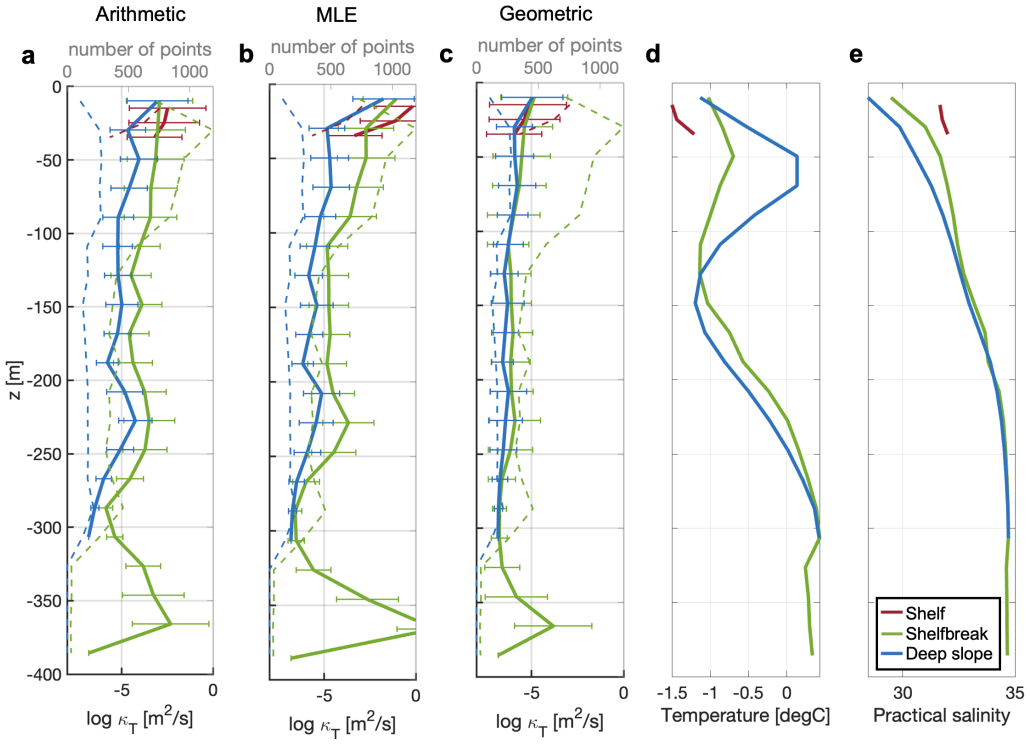

Figure 9. Bin averaged κ_T profiles at the shelf, shelfbreak, and deep slope regions using (a) an arithmetic average, (b) an MLE, and (c) a geometric average. Here κ_T is calculated using the FS method. Dashed lines indicate number of data points in each depth bin (corresponding the to upper x-axis). Bin size is 10 m for the shelf and 20 m for the shelfbreak and deep slope. Error bars are calculated as standard deviation in log space within each bin. Arithmetically averaged temperature (d) and salinity (e) profiles are also shown. A constant molecular diffusivity ($\kappa = 1.5 \times 10^{-7}$ m^{2}s^{-1}) is imposed at the location of any spectrum with both $|d\overline{T}/dz| > 0.001$ $^\circ$Cm^{-1} and SNR below the rejection threshold.

Table 1. Average κ_T (units m^2s^{-1}) over all depth bins calculated three ways (arithmetic mean, MLE, geometric mean) for three regions (shelf, shelfbreak, deep slope).

	Shelf	**Shelfbreak**	**Deep**
Arithmetic	1.9×10^{-3}	4.3×10^{-4}	5.2×10^{-5}
MLE	2.1×10^{-2}	2.9×10^{-4}	6.3×10^{-6}
Geometric	2.3×10^{-6}	1.4×10^{-6}	5.7×10^{-7}

as MLE) are included (Fig. 9 a-c). The MLE is calculated according to Baker and Gibson (1987), who showed that the MLE is less likely to underestimate log-normally distributed turbulent parameters, which are intermittent in time and space, compared to an arithmetic mean, when sample size is small. We have already shown that the distribution of κ_T is approximately log-skew-normal, which may have implications for the choice in averaging method. Davis (1996) argued that the arithmetic mean may be the most reliable when the sample distribution is uncertain, compared to other methods (e.g. using the MLE) that assume a lognormal distribution, especially when the sample size is small. It is not the intent here to identify any one averaging method as better than another, but, for the purpose of future comparisons, the outcomes from each are included.

There is a clear correlation between bottom depth and κ_T throughout the water column for the arithmetic average and the MLE, in which the shelf and shelfbreak profiles exhibit enhanced turbulent diffusivity by up to 1-2 orders of magnitude at the same water depths compared to the deep slope profiles. In the deep slope averages, κ_T is typically between 10^{-6} and 10^{-5} m^2s^{-1} between 100-200 m—a range of depths that encompasses the cold halocline—which is consistent with observations of κ_T from Fer (2009) throughout the cold halocline in the Amundsen Basin. However, error bars are large due to the inherent patchiness of turbulence, and we have omitted the shallowest and deepest bin for the averaged shelf profiles in Fig. 9 since nearly all observations within these bins were either rejected or set to molecular diffusivity due to low SNR. The geometrically averaged profiles do not vary in κ_T to the same extent between the shelf, shelfbreak, and deep slope.

Mean turbulent temperature diffusivities through the full range of measured depths at the shelf, shelfbreak, and deep slope are shown in Table 1 for each averaging method. Using an arithmetic mean and MLE, there is approximately one to two order of magnitude decrease in κ_T on the shelf versus shelfbreak, and on the shelfbreak versus deep slope. Using a geometric mean yields similar κ_T on the shelf and shelfbreak, and an order of magnitude decrease over the deep slope.

For the majority of their observations, Schulz et al. (2023) reported average vertical diffusivity during the MOSAiC expedition (see Rabe et al., 2022) to be largest using an arithmetic and smallest using a geometric mean, with the MLE typically having magnitude somewhere in between. This trend is also observed over the deep slope, which is the depth region most similar to the mid-basin environment where the MOSAiC observations were made. The geometrically averaged κ_T is smaller than the arithmetic mean and MLE in all three depth regions, as is expected for a log-normally distributed variable. In contrast, the MLE is about one order of magnitude larger than the arithmetic mean on the shelf and shelfbreak.

The number of κ_T estimates used in each bin is indicated by the dashed lines in Fig. 9. For instance, few profiles achieved maximum depths below 300 m, so for these bins, the estimates of κ_T are poor representatives of averages. Similarly, there were few profiles on the shelfbreak that reached maximum depths $\geq$ 40 m.

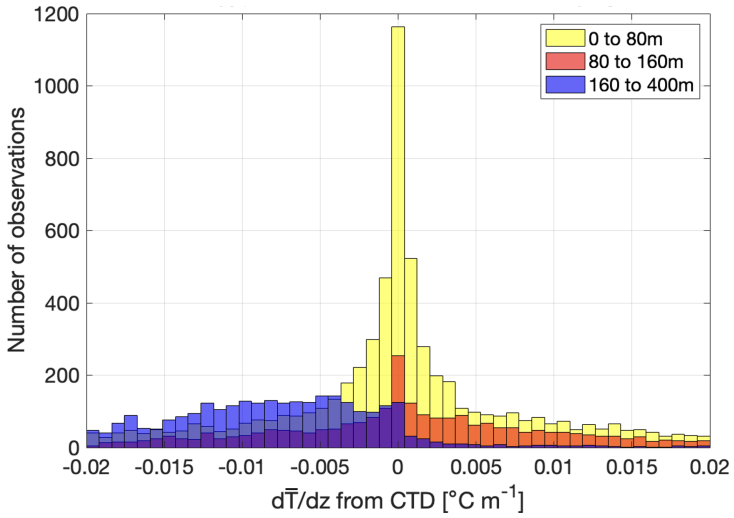

Figure 10. Histogram of background $d\overline{T}/dz$, measured from the CTD, colour-coded by depth range. Only the 95 profiles with working MR are included.

4.4 Background temperature and heat flux

Temperature gradients at 10-100 m scales across the study region are correlated with three distinct ocean layers (Fig. 10). In the region 0 to 80 m, gradients are very small (most measurements have magnitude $< 5 \times 10^{-3}$ °Cm^{-1}) and are normally distributed about zero. This region represents the surface layer, and is comprised of several distinct water masses: newly formed cold winter water on the shelf, a surface mixed layer in the basin away from the shelf, and warm remnant PSW. These different water masses are distinguishable by background temperature in section KTO (Fig. 1). Due to its composite nature, the surface layer is patchy with respect to temperature, and it is thus not surprising that both positive and negative $d\overline{T}/dz$ are present. Between 80 and 160 m, the distribution of $d\overline{T}/dz$ peaks near zero with long tails in both the positive and negative directions. This is the depth region corresponding to the cold halocline. At 160 m and below, the background temperature gradient is almost always negative and, unlike at depths < 160 m, the distribution does not peak near zero. This strong signal of negative $d\overline{T}/dz$ is due to the warm and salty AW.

Heat exchanges between water masses in the Arctic Ocean (e.g., between warm AW and the overlying cold halocline) can affect water mass properties as well as sea ice formation and melt, with implications for global climate systems (e.g., Maykut & Untersteiner, 1971; Polyakov et al., 2020; Rippeth et al., 2015). Estimates of turbulent diffusivity and heat flux are therefore important for understanding the dynamics of the region. Heat flux, $\mathcal{F}$, is linearly related to both the background temperature gradient and the temperature diffusivity:

$$\mathcal{F} = -\kappa_T \frac{d\overline{T}}{dz} C_p \rho, \tag{12}$$

where C_p and ρ are the specific heat capacity and the in-situ density of sea water. Note that heat flux is defined so that negative $d\overline{T}/dz$ (the spatially averaged vertical temperature gradient) yields a positive flux, which implies an upward transport of heat.

Heat flux distributions are separated into depth ranges in Fig. 11. The heat fluxes with the largest magnitudes (> 10 Wm^{-2}) are seen most often in the 0-80 m depth cat-

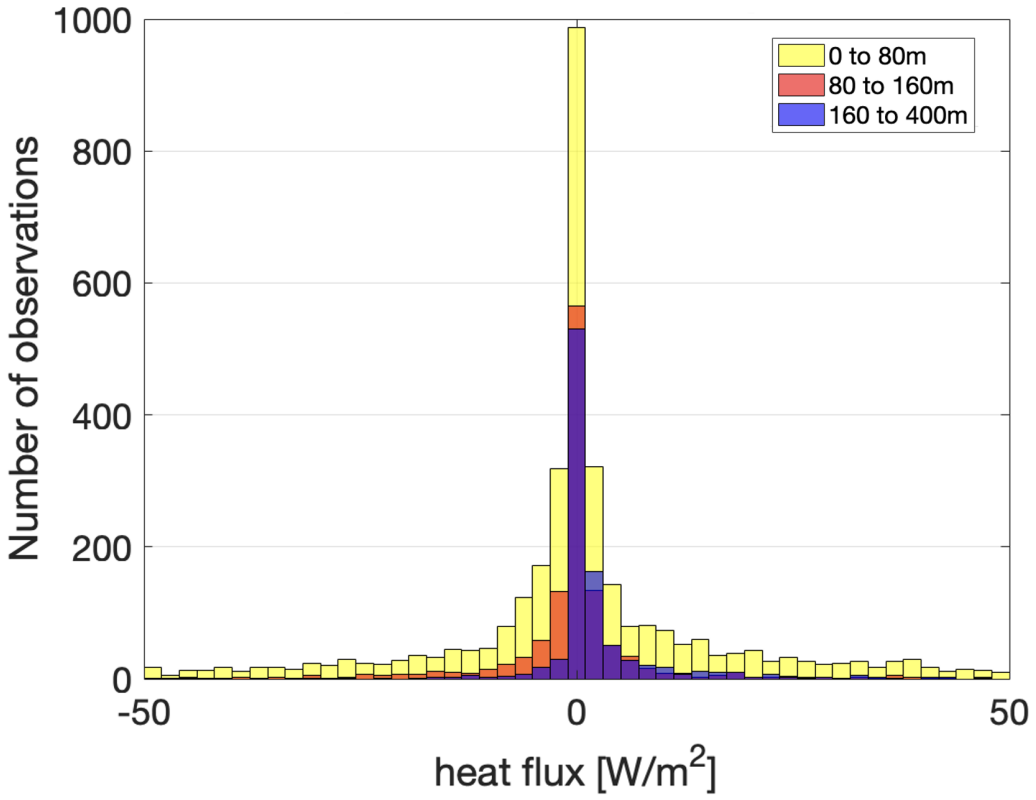

Figure 11. Histogram of heat flux in three depth ranges. Only observations with SNR above the rejection threshold are included. Heat fluxes are calculated from $\kappa_{T,FS}$.

egory, and only rarely at depths > 80 m. This is likely because the surface waters tend to exhibit the largest κ_T and also tend to be patchy in temperature, which can result in sharp gradients and large heat fluxes. In the deeper and typically less energetic waters, the heat flux magnitudes tend to be smaller. The 80-160 m fluxes peak around 0 Wm^{-2}, while the peak of the 160-400 m fluxes is shifted slightly toward positive values, since these deepest observations are associated with almost exclusively negative $d\overline{T}/dz$ (Fig. 10) and thus upward heat flux.

4.4.1 Heat flux into the cold halocline at the AW thermocline

Heat flux into the cold halocline was calculated for individual profiles following a similar method to Rippeth et al. (2015) in which an average κ_T is estimated for an entire layer, along with a bulk mean temperature gradient that approximates $\frac{d\overline{T}}{dz} \approx \frac{\Delta T}{\Delta Z}$, where ΔZ is the layer thickness and ΔT is the potential temperature difference between the top and bottom of the layer. Arithmetic averages are used for the sake of comparison with other literature. The core of the cold halocline was defined for each profile to be the depth at which the lowest temperature was observed, between the 1026 and 1027 $\mathrm{kg/m}^3$ isopycnals. We then calculated the mean heat flux into the cold halocline above and below its core using bulk temperature gradients and averaged κ_T over the upper and lower portions of the cold halocline. An average heat flux into the cold halocline from above (below) of -2.8±2.8 Wm^{-2} (1.2±3.0 Wm^{-2}) was calculated from 15 profiles with maximum depth greater than the base of the cold halocline. Thus, net inward heat flux is estimated as 4.0±4.1 Wm^{-2}, with a slightly larger amount of heat entering from the

surface, rather than the deeper ocean, at this time of year. This inward heat flux would eventually erode the cold halocline in the absence of seasonally inflowing cold, salty water from ice formation upstream on the Bering and Chukchi shelves (e.g., Itoh et al., 2012; Pacini et al., 2019), or locally on the Beaufort shelf (Dabrowski et al., 2022; Jackson et al., 2015).

Heat flux through the upper bound of the AW varies throughout the Arctic Ocean. Our average upward flux of 1.2±3.0 Wm^{-2} through the AW thermocline is smaller than the mean heat flux across the AW thermocline of 22±2 Wm^{-2} reported in Rippeth et al. (2015) at the continental slope north of Svalbard. Renner et al. (2018) and Meyer et al. (2017) also report relatively large heat fluxes (> 10 Wm^{-2}) above the AW core in the Nansen Basin, and both Polyakov et al. (2019) and Schulz, Janout, et al. (2021) report fluxes of 3-4 Wm^{-2} near slope regions in the Eurasian Basin. In the Amundsen Basin away from steep bathymetry, smaller heat fluxes of $\mathcal{O}(0.1)$ Wm^{-2} have been observed (Fer, 2009; Guthrie et al., 2017).

In many cases (e.g., Peterson et al., 2017; Meyer et al., 2017; Renner et al., 2018), episodically high Arctic Ocean heat fluxes one or more orders of magnitude larger than annual averages have been observed, and have been associated with storm events, AW shoaling, and seasonal ice melt. In the present Canada Basin dataset, some large upward fluxes at the top of the AW on the order of 10 Wm^{-2} are also observed. Such variability, combined with the relatively small number of profiles that reached AW depth, contributes to the large uncertainty associated with our estimates of AW thermocline flux and net flux into the cold halocline.

4.4.2 Statistics of heat fluxes throughout the surface, cold halocline, and AW layers

The distributions of heat flux throughout the surface layer, the cold halocline, and the AW are now considered (Fig. 12). These layers, which are visible in the example section shown in Fig. 1a, are defined as follows:

- **Surface layer water**, which includes newly formed winter water, mixed layer basin water, and PSW: density less than 1026 kg m^{-3} and practical salinity less than 31.5
- **Cold halocline water**: density between 1026 and 1027 kg m^{-3}, or temperature below -1 °C and depth below 75 m
- **AW**: depth below 150 m and practical salinity greater than 34

These definitions are based on empirical estimates of distinct water masses after examining the salinity, temperature, and density background across multiple sections. The conditions for each water mass deliberately do not overlap—that is, there are some data points that do not fall into any of the three categories. Such points occur most often at interfaces where characteristics are mixed between two water masses. Using these narrow definitions allows for more confidence in water mass classification, compared to classification by depth only. As a result, the number of heat flux estimates is smaller when classifying by water mass compared to Fig. 11 where all non-rejected estimates are included.

Surface waters exhibit both positive and negative heat fluxes with a slight bias toward positive (Fig. 12a). The nearest surface waters would likely have been cooling due to air-sea heat fluxes at the time of year when these measurements were made, causing such an upward flux of heat towards shallower depths. The observation of occasional upward heat fluxes of 10-50 Wm^{-2} above the warm PSW is notable, since even highly intermittent fluxes of this magnitude could lead to warming of the cool surface layer and delayed freeze-up. Within the cold halocline layer (Fig. 12b), the heat flux distribution

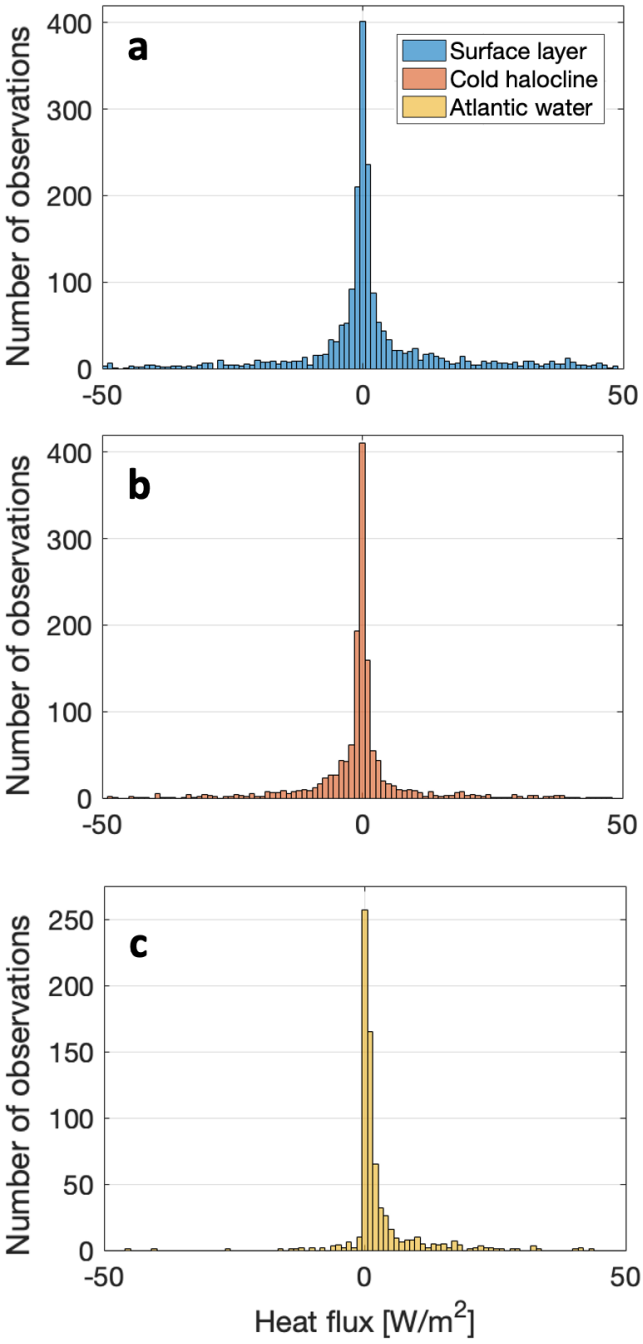

Figure 12. Heat flux distributions for three distinct water masses: a) the surface layer, b) the cold halocline, and c) the AW. Positive heat flux corresponds to upward heat transport. Only observations with SNR above the rejection threshold are included. Heat fluxes are calculated from $\kappa_{T,FS}$.

is approximately centered about 0 Wm^{-2}, indicating that a similar amount of heat is transported downward into the cold halocline from the surface layer (accounting for the negative fluxes) and upward from the AW layer (accounting for the positive fluxes), consistent with the findings of Schulz, Janout, et al. (2021) in the eastern Arctic. This represents a net warming of the cold halocline and is consistent with the layer-averaged halocline heat flux calculation described earlier in this section. In the surface and cold halocline layers, most heat fluxes have magnitude 10 Wm^{-2} or less, with some larger fluxes >50 Wm^{-2} that comprise approximately 15% of the surface layer observations (representing 8% of the observations overall). Within the AW layer (Fig. 12c), such larger heat fluxes are less common due to smaller temperature gradients. Heat flux throughout the AW is almost always upward, since the temperature of this water mass is elevated compared to the overlying cold halocline and none of the profiles were deep enough to see the temperature gradients reverse sign below the AW core.

The turbulent heat fluxes from this near-coastal data set tend to be larger by about 1-2 orders of magnitude in comparison to the double diffusive heat fluxes in the central Canada Basin calculated by Timmermans et al. (2008). Shaw and Stanton (2014) reported turbulent heat fluxes as high as 2 Wm^{-2} near the Northwind Ridge to the west of the Canada Basin, comparable to our median values of heat flux near the shelfbreak. The small number of large (>10 Wm^{-2}) heat fluxes observed in this work may be the result of intermittent turbulence-generating events as flows interact with the steep shelfbreak bathymetry; the importance of boundary layers in mixing at the basin scale has has been previously demonstrated with microstructure measurements and tracer release experiments (e.g., Ledwell & Hickey, 1995; Holtermann & Umlauf, 2012), and some possible mechanisms for the conversion of unsteady lee wave energy to turbulence at boundaries in Arctic shelf seas have been proposed (e.g., Fer et al., 2020; Schulz, Büttner, et al., 2021). More comprehensive measurements in the future could clarify the frequency with which such fluxes occur, and the processes that generate them.

5 Conclusions

A total of 95 temperature microstructure profiles were obtained on the shelf and in the vicinity of the shelfbreak of the southern Canada Basin by attaching a microstructure probe to a CTD rosette during an autumn 2018 research cruise. We compared two methods (FS and RW) for estimating turbulence parameters χ and ε, after applying several rigorous quality control measures.

The quality control framework developed in this work assesses the signal-to-noise ratio, the quality of the spectral fit to the Kraichnan form, and the potential for contamination due to sudden instrument deceleration. No double diffusive steps were observed, and low (~ 0.5 ms^{-1}) instrument descent rates were maintained in this dataset. The FS and RW methods were found to yield similar results for χ after rejection criteria were applied to this particular dataset. Any future work involving ε and χ should consider the potential impact of DD instability, possibly by implementing a rejection criterion based on R_ρ. The differences in the two methods suggest that the FS method is preferred for estimates of χ and ε when DD is involved and when ε is sufficiently small (such that k_B can be reliably estimated using a FS fit). The RW method is likely to be more accurate when ε is large and when shear instability (rather than DD) dominates. We hypothesize that the two methods will provide consistent estimates when ε is small and when DD processes are weak, and that neither method should be applied when ε is large and DD is observed.

Estimates of turbulent diffusivity were, on average, elevated in profiles obtained over shallower bathymetry compared to those obtained over the deep slope. We also examined background temperature gradients and determined that three distinct layers in this region—the surface layer, the cold halocline, and the warm AW—could be charac-

terized via $d\overline{T}/dz$. Vertical heat fluxes obtained from diffusivities were calculated for the three layers. Surface layer heat fluxes were both positive (upward) and negative (downward) with a slight bias toward positive. Heat fluxing into the cold halocline from above was found to be of the same order of magnitude as heat flux from the underlying AW. In both the surface and cold halocline, heat fluxes tended to be within ± 10 Wm^{-2}, but were occasionally several times larger. In the AW layer, temperature gradients are more stable, and thus $\mathcal{O}(10)$ Wm^{-2} heat fluxes were observed less often compared to the overlying layers.

Our results support the measurement of temperature microstructure on routine hydrographic surveys, since data can be used to estimate turbulent heat fluxes provided that strict rejection criteria are applied. Estimations of heat flux are important for constraining heat budgets and therefore making predictions about sea ice formation and loss over time. Repeated measurements of this nature in the Canada Basin and throughout the Arctic Ocean could increase the breadth of observations in this unique and rapidly changing environment.

Appendix A Additional details on the rejection criteria

A1 Mean absolute deviation (MAD)

MAD rejection occurs when the observed spectrum does not resemble the Kraichnan spectrum. This may happen when flow is laminar or nearly laminar (that is, when turbulent diffusivities approach molecular values), or when environmental processes other than turbulence are present. Varying degrees of anisotropy in the turbulent field, often relating to the effect of stratification on the vertical dimension, can also influence how well an observed spectrum adheres to the theoretical form (Gargett, 1985). Thus, it is not always appropriate to fit a Kraichnan spectrum and doing so in these cases will likely yield unreliable estimates of the true environmental turbulence.

For fits made using the FS method, MAD is calculated using every wavenumber; for fits made using the RW method, the region over which MAD is calculated is limited to the region of the fit. The criterion of rejection when MAD > 1.4 comes from the recommended threshold of $2(2/d)^{1/2}$ where $d = 4$, the number of degrees of freedom (Ruddick et al., 2000).

A2 Descent rate

Spectra that are contaminated due to sudden rosette deceleration will measure elevated non-enironmental turbulence (Goto et al., 2018). The instrument descent speed, w, varies across profiles because the maximum depths reached by profiles in this dataset range between 20 m and 400 m. Thus, a constant rejection threshold is not appropriate. In Equation 11, the coefficient 0.75 and the 3 s averaging window were chosen after comparing MR temperature gradient variance from rejected portions of profiles to variance prior to the deceleration for multiple different averaging window sizes and coefficients.

We define the following variance ratio to test the effectiveness of the descent speed rejection criterion:

$$\text{Variance ratio} = \frac{\text{var}(\nabla T'_{\text{before}})}{\text{var}(\nabla T'_{1s,\ \text{rejected}})} \tag{A1}$$

Here, $\text{var}(\nabla T'_{\text{before}})$ is the variance of the temperature gradient fluctuations in the n-seconds prior to the start of a profile segment rejected by the descent rate criterion, where n defines the period of time used for the averaging window against which a given

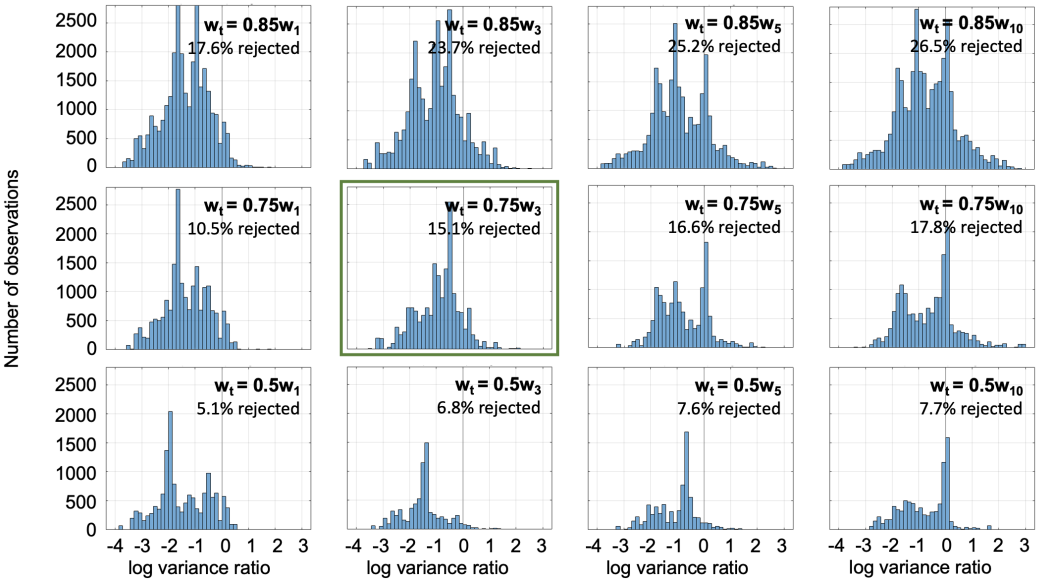

Figure A1. Histograms of the base 10 logarithm of variance ratio for various rejection thresholds at all descent rate-rejected segments. From left to right, averaging periods for the comparison segment in each column are 1, 3, 4, and 10 s. The vertical black line indicates where variance ratio = 1: if the threshold is effective, most data should fall to the left of this line. The threshold that was ultimately chosen (and its associated histogram) is indicated by the green box.

spectrum's descent rate is compared. For example, in Equation 11, $n = 3$. $\mathrm{var}(\nabla T'_{1s,\ \mathrm{rejected}})$ is the variance of the temperature gradient in a 1 s window within a segment rejected due to descent rate. When the rejection threshold for descent speed, w_t, is correctly defined, the variance ratio should be < 1 most of the time, since periods of abrupt deceleration exhibit enhanced temperature gradient variance due to turbulence compared to periods unaffected by deceleration.

Histograms of variance ratio for all descent speed-rejected segments are shown in Fig. A1, with different w_t. Averaging periods for the comparison segment (prior to deceleration) of 1, 3, 5, and 10 s (columns, Fig. A1) were tested, and it was observed that using 5 and 10s segments caused a notable increase in number of rejected segments with variance ratio >1, especially for $w_t = 0.75w_n$ and $w_t = 0.85w_n$. The difference in number of segments with variance ratio >1 is less obvious between averaging windows of 1 and 3s. However, to reduce the potentially biasing impact of short-lived ($<$ 1s duration) turbulent events, we decided to use the longer averaging period of 3s.

We additionally reject all spectra from 1.5s after w increases back above w_t. This overshoot of 1.5s is a conservative estimate based on the observation that segments of profiles affected by deceleration contamination take at most 1.5 seconds to return to their baseline after a slowing event.

For a 3s averaging window, the rejection threshold is w_3 multiplied by some coefficient. The variance ratio was calculated for various coefficients (rows, Fig. A1). Approximately 10% more rejection occurs when the threshold is defined with coefficient 0.75 compared to 0.5, and there is similarly an increase around 10% between 0.85 and 0.75 times. However, most of the additional rejection between the 0.5 and 0.75 thresholds occurs at variance ratio < 1. Thus, this rejection is probably warranted, since most rejected portions exhibit enhanced variance in $\nabla T'$. At the 0.85 threshold, there are a notable

771 number of rejected segments with variance ratio > 1, suggesting this threshold may be
772 too aggressive. 0.75 is then most appropriate, yielding the descent rate threshold defined
773 in Equation 11: $w_t = 0.75w_3$.

774 A3 Signal-to-noise ratio (SNR)

775 SNR is a property of the spectrum and does not depend on whether the FS or RW
776 method is used, but we observed an artificial lower limit for χ_{FS} that is influenced by
777 SNR and was used to determine our choice of rejection threshold. This limit is seen only
778 with the FS method since instrument noise is considered only when fitting to all wavenum-
779 bers. When the signal is low (and SNR is also low), the FS method often incorrectly fits
780 the peak of the theoretical spectrum to the noise peak (Fig. 3b), resulting in a χ that
781 is unrealistically large. This problem does not occur with the RW method, where the
782 wavenumbers over which the noise spectrum is significant are not considered when per-
783 forming the fit. However, the SNR rejection criterion is applied to all spectra irrespec-
784 tive of method, since low signal is indicative of low temperature variance (due to either
785 low turbulence or a well-mixed background, or both), and our methods for determining
786 χ and ε rely on the presence of sufficiently strong temperature variance.

787 Our rejection criterion of SNR < 2 is slightly stricter than Goto et al. (2018), who
788 reject spectra with SNR < 1.5. However, in comparing the results between the two meth-
789 ods, the lower limit on χ_{FS} was improved using the stricter rejection requirement of SNR
790 < 2 (Fig. 3a).

791 A4 Method difference

792 The choice of rejection threshold for FS and RW disagreement must be a balance
793 between including only trustworthy observations where the methods agree, and minimiz-
794 ing the amount of data lost. We have set the threshold such that rejection occurs when
795 the methods disagree by an order of magnitude, resulting in approximately 10% rejec-
796 tion. However, if the threshold was to be implemented for method disagreements greater
797 than a factor of 5, 17% of data would be rejected; for a factor of 3, $\sim$25% would be re-
798 jected.

799 Appendix B Descent rate limits on ε_{FS}

800 The maximum resolvable wavenumber in cpm depends on the Nyquist frequency,
801 which is one half of the sample frequency, f_s, and descent rate, w:

$$802 \qquad k_{max} = \frac{(\frac{1}{2}f_s)}{w}. \tag{B1}$$

803 The maximum resolvable wavenumber limit is relevant to the FS method, which
804 calculates ε from an estimate of k_B. In contrast, the RW method does not require es-
805 timates of k_B, and spectral values near k_B are not used in the RW fitting algorithm. From
806 Equations 6 and B1, the theoretical maximum resolvable ε when using the FS method
807 depends on descent rate as

$$808 \qquad \varepsilon_{max,FS} = \left(2\pi\frac{(\frac{1}{2}f_s)}{w}\right)^4 \nu\kappa^2, \tag{B2}$$

809 assuming that k_B must be fully resolved for an accurate estimate.

810 When plotted against the scattered data ε versus w, $\varepsilon_{max,FS}$ (green curve in Fig.
811 B1) reproduces the shape of the upper limit of the observed ε_{FS} (red dashed curve in

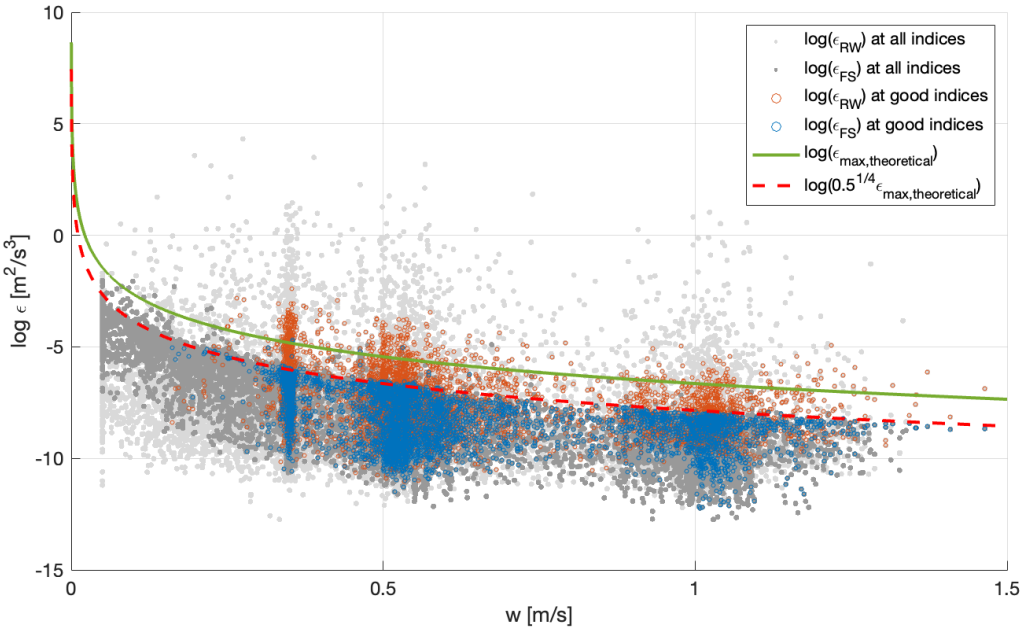

Figure B1. Both $\log \varepsilon$ from FS and RW plotted against instrument descent speed. ε_{FS} is limited by fall speed while ε_{RW} is not. $\varepsilon_{max,theoretical}$ (green) assumes k_B must be fully resolved to obtain an accurate estimate of ε, and thus depends on sample frequency (512Hz in this study). Observations indicate that the true limit for ε_{FS} is $0.5^{1/4}$ times the predicted theoretical limit.

Fig. B1), but is displaced downward, corresponding to $k_{max} = 2k_B$. This suggests that $k > 2k_B$ is required in order to be able to use the FS method for estimating ε.

Acronyms

CTD Conductivity-temperature-depth package
ADCP Acoustic Doppler current profiler
IBCAOv3 International Bathymetric Chart of the Arctic Ocean Version 3.0
AW Atlantic water
PSW Pacific summer water
MR MicroRider-1000
FS Full-spectrum
MLE Maximum Likelihood Estimate
RW Resolved wavenumber
SNR Signal-to-noise ratio
MAD Mean absolute deviation
DD Double diffusion

Open Research Section

The unprocessed profiles obtained using the Microrider-1000 in .P file format and processed profiles of turbulent diffusivity with corresponding CTD and position in .nc file format can be accessed on Borealis (Musgrave & Yee, 2023). The echosounder and shipboard ADCP data for the cruise HLY1803 were used to create this manuscript (Pickart,

Robert, 2018). The MATLAB code used for the RW method is publicly available (Ocean Mixing Group (Oregon State University), 2020).

Acknowledgments

We would like to thank two anonymous reviewers and the editor for their valuable comments that improved this manuscript. RY acknowledges funding from a Nova Scotia Graduate Scholarship, a NSERC Undergraduate Student Research Award, and the Ocean Frontier Institute. This research was undertaken, in part, thanks to funding from the Canada Research Chairs Program, and the Postdoctoral Scholar Program at the Woods Hole Oceanographic Institution. RP acknowledges US National Science Foundation grant OPP-1733564. Thank you to Barry Ruddick for sharing MLE spectral fitting code. We also thank Leah McRaven for processing the CTD data, Gianluca Meneghello and Nicholas Foukal for aiding in the collection of data for this study, and the captain and crew of the USCGS *Healy*.

References

Baker, M. A., & Gibson, C. H. (1987). Sampling Turbulence in the Stratified Ocean: Statistical Consequences of Strong Intermittency. *J. Phys. Oceanogr.*, *17*(10), 1817–1836. doi: 10.1175/1520-0485(1987)017⟨1817:STITSO⟩2.0.CO;2

Batchelor, G. K. (1959). Small-scale variation of convected quantities like temperature in turbulent fluid Part 1. General discussion and the case of small conductivity. *J. Fluid Mech.*, *5*(01), 113. doi: 10.1017/S002211205900009X

Bluteau, C. E., Lueck, R. G., Ivey, G. N., & Jones, N. L. (2017). Determining Mixing Rates from Concurrent Temperature and Velocity Measurements. *J. Atmos. Oceanic Technol.*, *34*, 11. doi: 10.1175/JTECH-D-16-0250.1

Brandt, P., Bange, H. W., Banyte, D., Dengler, M., Didwischus, S.-H., Fischer, T., ... Visbeck, M. (2015). On the role of circulation and mixing in the ventilation of oxygen minimum zones with a focus on the eastern tropical North Atlantic. *Biogeosciences*, *12*(2), 489–512. (Publisher: Copernicus GmbH) doi: 10.5194/bg-12-489-2015

Cael, B., & Mashayek, A. (2021). Log-Skew-Normality of Ocean Turbulence. *Phys. Rev. Lett.*, *126*(22), 224502. doi: 10.1103/PhysRevLett.126.224502

Dabrowski, J. S., Pickart, R. S., Stockwell, D. A., Lin, P., & Charette, M. A. (2022). Physical drivers of sediment-water interaction on the Beaufort Sea shelf. *Deep Sea Res. Part I Oceanogr. Res. Pap.*, *181*, 103700. doi: 10.1016/j.dsr.2022.103700

Davis, R. E. (1996). Sampling Turbulent Dissipation. *J. Phys. Oceanogr.*, *26*(3), 341–358. doi: 10.1175/1520-0485(1996)026⟨0341:STD⟩2.0.CO;2

Dosser, H. V., Chanona, M., Waterman, S., Shibley, N. C., & Timmermans, M.-L. (2021). Changes in Internal Wave-Driven Mixing Across the Arctic Ocean: Finescale Estimates From an 18-Year Pan-Arctic Record. *Geophys. Res. Lett.*, *48*(8), e2020GL091747. doi: 10.1029/2020GL091747

Dosser, H. V., & Rainville, L. (2016). Dynamics of the Changing Near-Inertial Internal Wave Field in the Arctic Ocean. *J. Phys. Oceanogr.*, *46*(2), 395–415. doi: 10.1175/JPO-D-15-0056.1

Fer, I. (2009). Weak Vertical Diffusion Allows Maintenance of Cold Halocline in the Central Arctic. *Atmos. Ocean. Sci. Lett.*, *2*(3), 148–152. doi: 10.1080/16742834.2009.11446789

Fer, I., Koenig, Z., Kozlov, I. E., Ostrowski, M., Rippeth, T. P., Padman, L., ... Kolås, E. (2020). Tidally Forced Lee Waves Drive Turbulent Mixing Along the Arctic Ocean Margins. *Geophys. Res. Lett.*, *47*(16), e2020GL088083. doi: 10.1029/2020GL088083

Fine, E. C., & Cole, S. T. (2022). Decadal Observations of Internal Wave Energy,

Shear, and Mixing in the Western Arctic Ocean. *J. Geophys. Res. Oceans*, *127*(5), e2021JC018056. doi: 10.1029/2021JC018056

Freilich, M. A., & Mahadevan, A. (2019). Decomposition of Vertical Velocity for Nutrient Transport in the Upper Ocean. *J. Phys. Oceanogr.*, *49*(6), 1561–1575. doi: 10.1175/JPO-D-19-0002.1

Gargett, A. E. (1985). Evolution of scalar spectra with the decay of turbulence in a stratified fluid. *J. Fluid Mech.*, *159*(-1), 379. doi: 10.1017/S0022112085003263

Gnanadesikan, A., Dunne, J. P., & John, J. (2012). Understanding why the volume of suboxic waters does not increase over centuries of global warming in an Earth System Model. *Biogeosciences*, *9*(3), 1159–1172. (Publisher: Copernicus GmbH) doi: 10.5194/bg-9-1159-2012

Goto, Y., Yasuda, I., & Nagasawa, M. (2016). Turbulence Estimation Using Fast-Response Thermistors Attached to a Free-Fall Vertical Microstructure Profiler. *J. Atmos. Oceanic Technol.*, *33*(10), 2065–2078. doi: 10.1175/JTECH-D-15-0220.1

Goto, Y., Yasuda, I., & Nagasawa, M. (2018). Comparison of Turbulence Intensity from CTD-Attached and Free-Fall Microstructure Profilers. *J. Atmos. Oceanic Technol.*, *35*(1), 147–162. doi: 10.1175/JTECH-D-17-0069.1

Goto, Y., Yasuda, I., Nagasawa, M., Kouketsu, S., & Nakano, T. (2021). Estimation of Basin-scale turbulence distribution in the North Pacific Ocean using CTD-attached thermistor measurements. *Sci. Rep.*, *11*. doi: 10.1038/s41598-020-80029-2

Gregg, M. C., & Meagher, T. B. (1980). The dynamic response of glass rod thermistors. *J. Geophys. Res.*, *85*(C5), 2779. doi: 10.1029/JC085iC05p02779

Guthrie, J. D., Fer, I., & Morison, J. H. (2017). Thermohaline staircases in the Amundsen Basin: Possible disruption by shear and mixing. *J. Geophys. Res. Oceans*, *122*(10), 7767–7782. doi: 10.1002/2017JC012993

Holmes, R. M., Moum, J. N., & Thomas, L. N. (2016). Evidence for seafloor-intensified mixing by surface-generated equatorial waves. *Geophys. Res. Lett.*, *43*(3), 1202–1210. doi: 10.1002/2015GL066472

Holtermann, P. L., & Umlauf, L. (2012). The Baltic Sea Tracer Release Experiment: 2. Mixing processes. *J. Geophys. Res. Oceans*, *117*(C1). doi: 10.1029/2011JC007445

Inoue, R., Yamazaki, H., Wolk, F., Kono, T., & Yoshida, J. (2007). An Estimation of Buoyancy Flux for a Mixture of Turbulence and Double Diffusion. *J. Phys. Oceanogr.*, *37*(3), 611–624. doi: 10.1175/JPO2996.1

Itoh, M., Shimada, K., Kamoshida, T., McLaughlin, F., Carmack, E., & Nishino, S. (2012). Interannual variability of Pacific Winter Water inflow through Barrow Canyon from 2000 to 2006. *J. Oceanogr.*, *68*(4), 575–592. doi: 10.1007/s10872-012-0120-1

Jackson, J. M., Melling, H., Lukovich, J. V., Fissel, D., & Barber, D. G. (2015). Formation of winter water on the Canadian Beaufort shelf: New insight from observations during 2009–2011. *J. Geophys. Res. Oceans*, *120*(6), 4090–4107. doi: 10.1002/2015JC010812

Jakobsson, M., Mayer, L., Coakley, B., Dowdeswell, J. A., Forbes, S., Fridman, B., ... Weatherall, P. (2012). The International Bathymetric Chart of the Arctic Ocean (IBCAO) Version 3.0. *Geophys. Res. Lett.*, *39*(12). doi: 10.1029/2012GL052219

Kraichnan, R. H. (1968). Small-scale structure of a scalar field convected by turbulence. *Phys. Fluids*, *11*(5), 945–953. doi: 10.1063/1.1692063

Ledwell, J. R., & Hickey, B. M. (1995). Evidence for enhanced boundary mixing in the Santa Monica Basin. *J. Geophys. Res. Oceans*, *100*(C10), 20665–20679. doi: 10.1029/94JC01182

Lele, R., Purkey, S. G., Nash, J. D., MacKinnon, J. A., Thurnherr, A. M., Whalen,

C. B., ... Talley, L. D. (2021). Abyssal Heat Budget in the Southwest Pacific Basin. *J. Phys. Oceanogr.*, *51*(11), 3317–3333. doi: 10.1175/JPO-D-21-0045.1

Lenn, Y.-D., Rippeth, T. P., Old, C. P., Bacon, S., Polyakov, I., Ivanov, V., & Hölemann, J. (2011). Intermittent Intense Turbulent Mixing under Ice in the Laptev Sea Continental Shelf. *J. Phys. Oceanogr.*, *41*(3), 531–547. doi: 10.1175/2010JPO4425.1

Lenn, Y. D., Wiles, P. J., Torres-Valdes, S., Abrahamsen, E. P., Rippeth, T. P., Simpson, J. H., ... Kirillov, S. (2009). Vertical mixing at intermediate depths in the Arctic boundary current. *Geophys. Res. Lett.*, *36*(5). doi: 10.1029/2008GL036792

Lin, P., Pickart, R. S., McRaven, L. T., Arrigo, K. R., Bahr, F., Lowry, K. E., ... Mordy, C. W. (2019). Water Mass Evolution and Circulation of the Northeastern Chukchi Sea in Summer: Implications for Nutrient Distributions. *J. Geophys. Res. Oceans*, *124*(7), 4416–4432. doi: 10.1029/2019JC015185

Lin, P., Pickart, R. S., Våge, K., & Li, J. (2021). Fate of Warm Pacific Water in the Arctic Basin. *Geophys. Res. Lett.*, *48*(20), e2021GL094693. doi: 10.1029/2021GL094693

Lincoln, B. J., Rippeth, T. P., Lenn, Y.-D., Timmermans, M. L., Williams, W. J., & Bacon, S. (2016). Wind-driven mixing at intermediate depths in an ice-free Arctic Ocean. *Geophys. Res. Lett.*, *43*(18), 9749–9756. doi: 10.1002/2016GL070454

Lueck, R. (2019). *RSI Technical Note 040: Noise in Temperature Gradient Measurements.* Rockland Scientific International Inc.

Lueck, R., Murowinski, E., & McMillan, J. (2020). *RSI Technical Note 039: A Guide to Data Processing.* Rockland Scientific International Inc.

Luketina, D. A., & Imberger, J. (2001). Determining Turbulent Kinetic Energy Dissipation from Batchelor Curve Fitting. *J. Atmos. Oceanic Technol.*, *18*(1), 100–113. doi: 10.1175/1520-0426(2001)018⟨0100:DTKEDF⟩2.0.CO;2

Maykut, G. A., & Untersteiner, N. (1971). Some results from a time-dependent thermodynamic model of sea ice. *J. Geophys. Res. (1896-1977)*, *76*(6), 1550–1575. doi: 10.1029/JC076i006p01550

Melet, A. V., Hallberg, R., & Marshall, D. P. (2022). The role of ocean mixing in the climate system. In M. Meredith & A. N. Garabato (Eds.), *Ocean mixing: drivers, mechanisms and impacts.* Elsevier.

Merrifield, S. T., Laurent, L. S., Owens, B., Thurnherr, A. M., & Toole, J. M. (2016). Enhanced Diapycnal Diffusivity in Intrusive Regions of the Drake Passage. *J. Phys. Oceanogr.*, *46*(4), 1309–1321. doi: 10.1175/JPO-D-15-0068.1

Meyer, A., Fer, I., Sundfjord, A., & Peterson, A. K. (2017). Mixing rates and vertical heat fluxes north of Svalbard from Arctic winter to spring. *J. Geophys. Res. Oceans*, *122*(6), 4569–4586. doi: 10.1002/2016JC012441

Morison, J. H., Long, C. E., & Levine, M. D. (1985). Internal wave dissipation under sea ice. *J. Geophys. Res. Oceans*, *90*(C6), 11959–11966. doi: 10.1029/JC090iC06p11959

Moum, J. N. (1996). Efficiency of mixing in the main thermocline. *J. Geophys. Res. Oceans*, *101*(C5), 12057–12069. doi: 10.1029/96JC00508

Moum, J. N., & Nash, J. D. (2009). Mixing Measurements on an Equatorial Ocean Mooring. *J. Atmos. Oceanic Technol.*, *26*(2), 317–336. doi: 10.1175/2008JTECHO617.1

Moum, J. N., Perlin, A., Nash, J. D., & McPhaden, M. J. (2013). Seasonal sea surface cooling in the equatorial Pacific cold tongue controlled by ocean mixing. *Nature*, *500*(7460), 64–67. doi: 10.1038/nature12363

Musgrave, R., & Yee, R. (2023). *Data to support publication: Turbulent diffusivity profiles on the shelf and slope at the southern edge of the Canada Basin [Dataset].* doi: 10.5683/SP3/79M1D3

Nash, J. D., Caldwell, D. R., Zelman, M. J., & Moum, J. N. (1999). A Thermocou-

ple Probe for High-Speed Temperature Measurement in the Ocean. *J. Atmos. Oceanic Technol.*, *16*(11), 1474–1482. doi: 10.1175/1520-0426(1999)016⟨1474:ATPFHS⟩2.0.CO;2

Nikolopoulos, A., Pickart, R. S., Fratantoni, P. S., Shimada, K., Torres, D. J., & Jones, E. P. (2009). The western Arctic boundary current at 152Â°W: Structure, variability, and transport. *Deep Sea Res. Part II Top. Stud. Oceanogr.*, *56*(17), 1164–1181. doi: 10.1016/j.dsr2.2008.10.014

Ocean Mixing Group (Oregon State University). (2020). *mixingsoftware.* `https://github.com/OceanMixingGroup`. (Accessed: 2020-05-29)

Osborn, T. R. (1980). Estimates of the Local Rate of Vertical Diffusion from Dissipation Measurements. *J. Phys. Oceanogr.*, *10*(1), 83–89. doi: 10.1175/1520-0485(1980)010⟨0083:EOTLRO⟩2.0.CO;2

Osborn, T. R., & Cox, C. S. (1972). Oceanic fine structure. *Geophys. Fluid Dyn.*, *3*(4), 321–345. doi: 10.1080/03091927208236085

Pacini, A., Moore, G. W. K., Pickart, R. S., Nobre, C., Bahr, F., Våge, K., & Arrigo, K. R. (2019). Characteristics and Transformation of Pacific Winter Water on the Chukchi Sea Shelf in Late Spring. *J. Geophys. Res. Oceans*, *124*(10), 7153–7177. doi: 10.1029/2019JC015261

Padman, L., & Dillon, T. M. (1989). Thermal microstructure and internal waves in the Canada Basin diffusive staircase. *Deep Sea Res. Part I Oceanogr. Res. Pap.*, *36*(4), 531–542. doi: 10.1016/0198-0149(89)90004-6

Padman, L., & Erofeeva, S. (2004). A barotropic inverse tidal model for the Arctic Ocean. *Geophys. Res. Lett.*, *31*(2). doi: 10.1029/2003GL019003

Peterson, A. K., Fer, I., McPhee, M. G., & Randelhoff, A. (2017). Turbulent heat and momentum fluxes in the upper ocean under Arctic sea ice. *J. Geophys. Res. Oceans*, *122*(2), 1439–1456. doi: 10.1002/2016JC012283

Pickart, R. S., Moore, G. W. K., Mao, C., Bahr, F., Nobre, C., & Weingartner, T. J. (2016). Circulation of winter water on the Chukchi shelf in early Summer. *Deep Sea Res. Part II Top. Stud. Oceanogr.*, *130*, 56–75. doi: 10.1016/j.dsr2.2016.05.001

Pickart, R. S., Moore, G. W. K., Torres, D. J., Fratantoni, P. S., Goldsmith, R. A., & Yang, J. (2009). Upwelling on the continental slope of the Alaskan Beaufort Sea: Storms, ice, and oceanographic response. *J. Geophys. Res. Oceans*, *114*(C1). doi: 10.1029/2008JC005009

Pickart, Robert. (2018). *HLY1803 [Dataset].* doi: 10.7284/908126

Polyakov, I. V., Padman, L., Lenn, Y.-D., Pnyushkov, A., Rember, R., & Ivanov, V. V. (2019). Eastern Arctic Ocean Diapycnal Heat Fluxes through Large Double-Diffusive Steps. *J. Phys. Oceanogr.*, *49*(1), 227–246. doi: 10.1175/JPO-D-18-0080.1

Polyakov, I. V., Rippeth, T. P., Fer, I., Alkire, M. B., Baumann, T. M., Carmack, E. C., ... Rember, R. (2020). Weakening of Cold Halocline Layer Exposes Sea Ice to Oceanic Heat in the Eastern Arctic Ocean. *J. Climate*, *33*(18), 8107–8123. doi: 10.1175/JCLI-D-19-0976.1

Rabe, B., Heuzé, C., Regnery, J., Aksenov, Y., Allerholt, J., Athanase, M., ... Zhu, J. (2022). Overview of the MOSAiC expedition: Physical oceanography. *Elem. Sci. Anth.*, *10*(1), 00062. doi: 10.1525/elementa.2021.00062

Rainville, L., & Winsor, P. (2008). Mixing across the Arctic Ocean: Microstructure observations during the Beringia 2005 Expedition. *Geophys. Res. Lett.*, *35*(8). doi: 10.1029/2008GL033532

Rainville, L., & Woodgate, R. A. (2009). Observations of internal wave generation in the seasonally ice-free Arctic. *Geophys. Res. Lett.*, *36*(23). doi: 10.1029/2009GL041291

Renner, A. H. H., Sundfjord, A., Janout, M. A., Ingvaldsen, R. B., Beszczynska-Möller, A., Pickart, R. S., & Pérez-Hernández, M. D. (2018). Variability and Redistribution of Heat in the Atlantic Water Boundary Current

North of Svalbard. *J. Geophys. Res. Oceans*, *123*(9), 6373–6391. doi: 10.1029/2018JC013814

Rippeth, T. P., Lincoln, B. J., Lenn, Y.-D., Green, J. A. M., Sundfjord, A., & Bacon, S. (2015). Tide-mediated warming of Arctic halocline by Atlantic heat fluxes over rough topography. *Nat. Geosci.*, *8*(3), 191–194. doi: 10.1038/ngeo2350

Ruddick, B., Anis, A., & Thompson, K. (2000). Maximum Likelihood Spectral Fitting: The Batchelor Spectrum. *J. Atmos. Oceanic Technol.*, *17*, 15. doi: 10.1175/1520-0426(2000)017⟨1541:MLSFTB⟩2.0.CO;2

Scheifele, B., Waterman, S., & Carpenter, J. R. (2021). Turbulence and Mixing in the Arctic Oceanâs Amundsen Gulf. *J. Phys. Oceanogr.*, *51*(1), 169–186. doi: 10.1175/JPO-D-20-0057.1

Scheifele, B., Waterman, S., Merckelbach, L., & Carpenter, J. R. (2018). Measuring the Dissipation Rate of Turbulent Kinetic Energy in Strongly Stratified, Low-Energy Environments: A Case Study From the Arctic Ocean. *J. Geophys. Res.*, 22. doi: 10.1029/2017JC013731

Schmitt, R. W. (1979). The growth rate of super-critical salt fingers. *Deep Sea Res. A*, *26*(1), 23–40. doi: 10.1016/0198-0149(79)90083-9

Schulz, K., Büttner, S., Rogge, A., Janout, M., Hölemann, J., & Rippeth, T. P. (2021). Turbulent Mixing and the Formation of an Intermediate Nepheloid Layer Above the Siberian Continental Shelf Break. *Geophys. Res. Lett.*, *48*(9), e2021GL092988. doi: 10.1029/2021GL092988

Schulz, K., Janout, M., Lenn, Y.-D., Ruiz-Castillo, E., Polyakov, I., Mohrholz, V., ... Vredenborg, M. (2021). On the Along-Slope Heat Loss of the Boundary Current in the Eastern Arctic Ocean. *J. Geophys. Res. Oceans*, *126*(2), e2020JC016375. doi: 10.1029/2020JC016375

Schulz, K., Kadko, D., Mohrholz, V., Stephens, M., & Fer, I. (2023). Winter Vertical Diffusion Rates in the Arctic Ocean, Estimated From 7Be Measurements and Dissipation Rate Profiles. *J. Geophys. Res. Oceans*, *128*(2), e2022JC019197. doi: 10.1029/2022JC019197

Shaw, W. J., & Stanton, T. P. (2014). Vertical diffusivity of the Western Arctic Ocean halocline. *J. Geophys. Res. Oceans*, *119*(8), 5017–5038. doi: 10.1002/2013JC009598

Simmons, H. L., Jayne, S. R., Laurent, L. C., & Weaver, A. J. (2004). Tidally driven mixing in a numerical model of the ocean general circulation. *Ocean Model.*, *6*(3-4), 245–263. doi: 10.1016/S1463-5003(03)00011-8

Spall, M. A., Pickart, R. S., Li, M., Itoh, M., Lin, P., Kikuchi, T., & Qi, Y. (2018). Transport of Pacific Water Into the Canada Basin and the Formation of the Chukchi Slope Current. *J. Geophys. Res. Oceans*, *123*(10), 7453–7471. doi: 10.1029/2018JC013825

St. Laurent, L., & Schmitt, R. W. (1999). The Contribution of Salt Fingers to Vertical Mixing in the North Atlantic Tracer Release Experiment. *J. Phys. Oceanogr.*, *29*(7), 1404–1424. doi: 10.1175/1520-0485(1999)029⟨1404:TCOSFT⟩2.0.CO;2

Timmermans, M.-L., & Marshall, J. (2019). Understanding Arctic Ocean Circulation: A Review of Ocean Dynamics in a Changing Climate. *Rev. Geophys.*, e2018JC014378. doi: 10.1029/2018JC014378@10.1002/(ISSN)1944-9208.GRANDCHAL1

Timmermans, M.-L., Toole, J., & Krishfield, R. (2018). Warming of the interior Arctic Ocean linked to sea ice losses at the basin margins. *Sci. Adv.*, *4*(8), eaat6773. doi: 10.1126/sciadv.aat6773

Timmermans, M.-L., Toole, J., Krishfield, R., & Winsor, P. (2008). Ice-Tethered Profiler observations of the double-diffusive staircase in the Canada Basin thermocline. *J. Geophys. Res. Oceans*, *113*(C1). doi: 10.1029/2008JC004829@10.1002/(ISSN)2169-9291.BEAUFORTG1

Uchida, T., Balwada, D., Abernathey, R., McKinley, G., Smith, S., & Lévy, M. (2019). The Contribution of Submesoscale over Mesoscale Eddy Iron Transport in the Open Southern Ocean. *Journal of Advances in Modeling Earth Systems*, *11*(12), 3934–3958. doi: 10.1029/2019MS001805

Warner, S. J., & Moum, J. N. (2019). Feedback of Mixing to ENSO Phase Change. *Geophys. Res. Lett.*, *46*(23), 13920–13927. doi: 10.1029/2019GL085415

Waterhouse, A. F., MacKinnon, J. A., Nash, J. D., Alford, M. H., Kunze, E., Simmons, H. L., ... Lee, C. M. (2014). Global Patterns of Diapycnal Mixing from Measurements of the Turbulent Dissipation Rate. *J. Phys. Oceanogr.*, *44*(7), 1854–1872. doi: 10.1175/JPO-D-13-0104.1

Woodgate, R. A., Weingartner, T., & Lindsay, R. (2010). The 2007 Bering Strait oceanic heat flux and anomalous Arctic sea-ice retreat. *Geophys. Res. Lett.*, *37*(1). doi: 10.1029/2009GL041621

Yu, X., Garabato, A. C. N., Martin, A. P., Buckingham, C. E., Brannigan, L., & Su, Z. (2019). An Annual Cycle of Submesoscale Vertical Flow and Restratification in the Upper Ocean. *J. Phys. Oceanogr.*, *49*(6), 1439–1461. doi: 10.1175/JPO-D-18-0253.1